

Revisiting the Giant Radio Galaxy ESO 422–G028: Part I. Discovery of a neutral inflow and recent star formation in a restarted giant

Henry R. M. Zovaro^{1*}, Chris J. Riseley^{2,3,4}, Philip Taylor^{1,6}, Nicole P. H. Nesvadba⁷, Tim J. Galvin^{4,5}, Umang Malik¹, Lisa J. Kewley^{1,6}

¹Research School of Astronomy and Astrophysics, The Australian National University, Canberra, ACT 2611, Australia

²Dipartimento di Fisica e Astronomia, Università degli Studi di Bologna, via P. Gobetti 93/2, 40129 Bologna, Italy

³INAF-Istituto di Radioastronomia, via P. Gobetti, 101, 40129 Bologna, Italy

⁴CSIRO Astronomy and Space Science, PO Box 1130, Bentley, WA 6102, Australia

⁵International Centre for Radio Astronomy Research, Curtin University, Bentley, WA 6102, Australia

⁶ARC Centre of Excellence for All Sky Astrophysics in 3 Dimensions (ASTRO 3D)

⁷Université de la Côte d’Azur, Observatoire de la Côte d’Azur, CNRS, Laboratoire Lagrange, Bd de l’Observatoire, CS 34229, 06304 Nice cedex 4, France

Accepted XXX. Received YYY; in original form ZZZ

ABSTRACT

Giant radio galaxies provide important clues into the life cycles and triggering mechanisms of radio jets. With large-scale jets spanning 1.8 Mpc, ESO 422–G028 ($z = 0.038$) is a giant radio galaxy that also exhibits signs of restarted jet activity in the form of pc-scale jets. We present a study of the spatially-resolved stellar and gas properties of ESO 422–G028 using optical integral field spectroscopy from the WiFeS spectrograph. In addition to the majority ~ 13 Gyr old stellar population, ESO 422–G028 exhibits a much younger ($\lesssim 10$ Myr old) component with an estimated mass of $10^{7.6} M_{\odot}$ which is predominantly located in the North-West region of the galaxy. Unusually, the ionised gas kinematics reveal two distinct disks traced by narrow ($\sigma_{\text{H}\alpha} < 100 \text{ km s}^{-1}$) and broad ($\sigma_{\text{H}\alpha} > 150 \text{ km s}^{-1}$) H α emission respectively. Both ionised gas disks are misaligned with the axis of stellar rotation, suggesting an external origin. This is consistent with the prominent interstellar NaD absorption, which traces a $1 - 3 M_{\odot} \text{ yr}^{-1}$ inflow of neutral gas from the North. We posit that an inflow of gas – either from an accretion event or a gas-rich merger – has triggered both the starburst and the restarted jet activity, and that ESO 422–G028 is potentially on the brink of an epoch of powerful AGN activity.

Key words: galaxies: individual: ESO 422–G028 – galaxies: active – galaxies: evolution – galaxies: ISM

1 INTRODUCTION

The largest single structures in the known Universe, Giant Radio Galaxies (GRGs) are radio galaxies with jets spanning distances greater than 0.7 Mpc in extent. First discovered by Willis et al. (1974), these giants are uncommon, with fewer than 1000 catalogued (Delhaize et al. 2021) and only a handful studied in detail. Typically hosted by early-type galaxies (ETGs), the largest known to-date is approximately 5 Mpc in size (Machalski et al. 2008), although only 15 per cent are larger than 2 Mpc (Dabhade et al. 2020a). A combination of long-lived or high-power periods of AGN activity (Subrahmanyan et al. 1996; Wiita et al. 1989) and low-density local environments (Mack et al. 1998; Malarecki et al. 2015) have been proposed as potential mechanisms enabling the jets to reach their gargantuan sizes.

In recent years, low-frequency radio surveys such as the MeerKAT International GHz Tiered Extragalactic Exploration (MIGHTEE; Jarvis et al. 2016) and the LOFAR Two-Metre Sky Survey (LoTSS; Shimwell et al. 2017) have led to the discovery

of hundreds of GRGs (Dabhade et al. 2020a,b; Delhaize et al. 2021), facilitating population studies of these rare objects. Despite the influx of new data, the precise conditions required to form these giant radio jets remains unclear. For example, Lan & Prochaska (2021) showed that GRGs do *not* preferentially reside in lower-density environments in comparison to “regular” radio galaxies; indeed, Dabhade et al. (2020a) found GRGs in field, group and cluster environments. Meanwhile, Dabhade et al. (2020b) found that GRGs tend to have lower Eddington ratios than their regular-sized counterparts, but similar supermassive black hole masses, suggesting the radiative efficiency of the accretion disk may be key to producing powerful jets. Additionally, roughly 5 per cent of GRGs are “double-double” sources with two sets of jets from different epochs of AGN activity (Dabhade et al. 2020a), suggesting that shortly-spaced episodes of AGN fuelling may also be important. Detailed studies of individual GRGs – including the properties of the host galaxy – are therefore crucial in elucidating the mechanisms that contribute to the growth of the jets. In particular, studying the fuel sources of GRGs may help us to figure out what is so special about these giants, and give us clues as to their life cycle.

Absorption lines are particularly useful for detecting inflows pow-

* E-mail: henry.zovaro@anu.edu.au

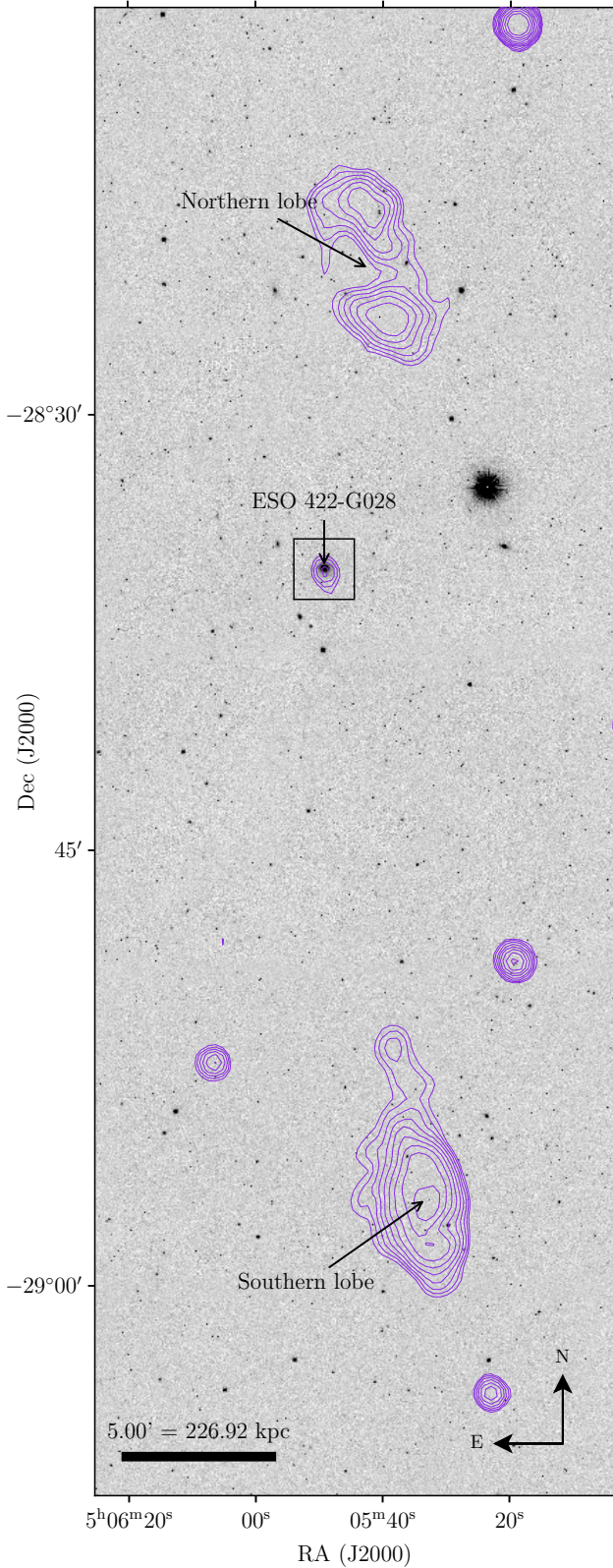


Figure 1. VISTA Hemisphere Survey *K*-band image (McMahon et al. 2013) showing ESO 422–G028 and its large-scale environment. The colour scaling of the image has been adjusted to enhance visibility of ESO 422–G028. The contours show the 1.4 GHz NRAO VLA Sky Survey (NVSS) image (Condon et al. 1998), revealing the Mpc-scale radio lobes, and represent 10 logarithmically spaced intervals from 3 mJy beam^{-1} to 50 mJy beam^{-1} . The box surrounding ESO 422–G028 shows the FoV of Fig. 2.

ering the jet activity, because gas can only be observed in absorption *in front of* the stellar continuum. As a result, inflows and outflows can be unambiguously identified, in contrast to emission lines: redshifted absorption traces gas flowing into the galaxy, and blueshifted absorption traces gas flowing out of the galaxy. At optical wavelengths, interstellar absorption by neutral sodium – the Na D doublet at 5889.9 \AA and 5895.9 \AA – can be used to detect inflows and outflows of neutral gas.

Although an estimated 1/3 of radio galaxies at $z < 0.2$ exhibit interstellar Na D absorption (Lehnert et al. 2011), in most cases it traces outflowing material. Similarly, H I is also most often observed in outflows (Morganti et al. 2005; Morganti & Oosterloo 2018). However, inflows of neutral gas traced by H I have been reported in radio galaxies (van Gorkom et al. 1989) and may fuel AGN activity. Moreover, a recent study by Roy et al. (2021a) found that redshifted interstellar Na D absorption appears to be common in quiescent intermediate-mass radio galaxies, suggesting such inflows can trigger the AGN.

The present work is part of a series of papers on the nearby GRG ESO 422–G028 ($z = 0.038150$; Jones et al. 2009), which exhibits lobes spanning approximately 1.8 Mpc that are no longer powered by the central engine (Subrahmanyan et al. 2008, hereafter S08). ESO 422–G028 also exhibits evidence for restarted jet activity in the form of pc-scale jets (Riseley et al., *in prep.*). In this paper we use high spectral resolution integral field spectroscopy to study the spatially resolved stellar and gas properties of ESO 422–G028. Our observations reveal a young stellar population in this GRG, plus complex ionised gas kinematics as traced by H α emission. We also detect prominent redshifted Na D absorption that traces an inflow, potentially fuelling both star formation and the restarted jet activity.

For the remainder of this paper we assume a flat Λ CDM cosmology with $\Omega_M = 0.3$, $\Omega_\Lambda = 0.7$ and $H_0 = 70 \text{ km s}^{-1} \text{ Mpc}^{-1}$. The coordinates and distances of ESO 422–G028 assumed in this work are given in Table 1.

2 THE GIANT RADIO GALAXY ESO 422–G028

Independently discovered to be a GRG in 1986 by both Saripalli et al. (1986) and Subrahmanya & Hunstead (1986), ESO 422–G028 is a nearby giant elliptical galaxy with radio lobes spanning a projected linear extent of 1.8 Mpc, with properties summarised in Table 1. As shown in Fig. 1, the radio source comprises two prominent FR II-type lobes extending roughly North–South and unresolved core emission centred on the host. The lobes are diffuse, with no prominent hotspots, and have ill-defined boundaries, indicating they are no longer being powered by the jet, with an estimated spectral age of 0.3 Gyr (S08).

Unusually for a GRG, the lobes are quite asymmetric, with a length ratio of 1:1.6. The Northern jet also bends to the West. At low frequencies, the backflow from the Northern lobe extends all the way back to the host, whilst that from the Southern lobe only reaches three quarters of the distance back towards the host (see fig. 8 of Beardsley et al. 2019). The Northern lobe exhibits a dramatic steepening of the spectral index towards its Northern boundary, contrary to what is typically observed in edge-brightened radio lobes, which S08 speculate is due to interaction with the more dense ambient medium in the North.

The kpc-resolution Very Large Array (VLA) image of S08, overlaid in Fig. 2, shows the collimated kpc-scale Southern jet and unresolved core emission. The relative brightness of the Southern jet compared to the Northern lobe indicates the Southern lobe is inclined towards the Earth. The VLA observations (project AS262, taken October 19 and 20 1986 in CnB configuration; see S08 for

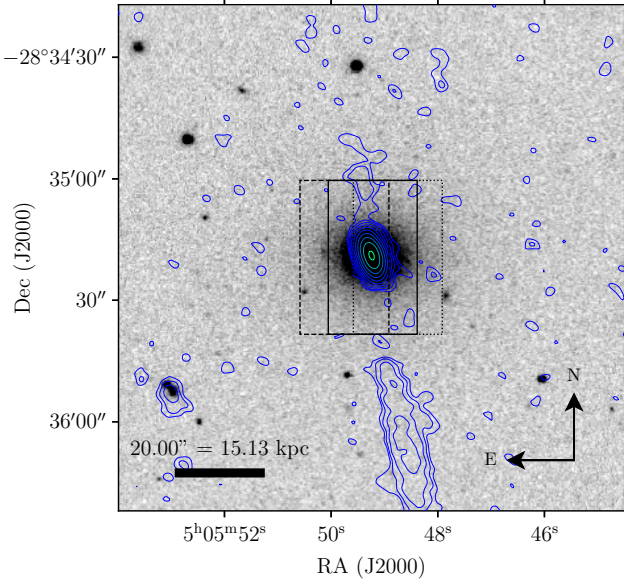


Figure 2. A zoom-in of the *VISTA* Hemisphere Survey *K*-band image (McMahon et al. 2013) indicated by the black box in Fig. 1. The solid, dashed and dotted boxes indicate the fields of view of our three different WiFeS pointings, and the contours show the 4.85 GHz VLA image representing 10 logarithmically-spaced intervals from 0.075 mJy beam^{−1} to 5.5 mJy beam^{−1}.

Table 1. Properties of ESO 422–G028 assumed in this paper.

Property	Value
RA (J2000)	05 ^h 05 ^m 49 ^s .22 ^a
Dec (J2000)	−28°35′19.4″ ^a
Redshift (<i>z</i>)	0.038150 ^b
Heliocentric recessional velocity	11437 km s ^{−1b}
Angular diameter distance (D_A)	156.02 Mpc
Luminosity distance (D_L)	168.15 Mpc
Stellar mass (M_*)	10 ^{11.4} M _⊙ ^c
BH mass (M_{BH})	1.7 ^{+0.4} _{−0.3} × 10 ⁹ M _⊙ ^c
Dust mass (M_{dust})	~ 10 ⁶ – 10 ⁷ M _⊙ ^d
Effective radius (R_e)	12.56 arcsec ^e
Star formation rate (SFR)	0.39 ± 0.01 M _⊙ yr ^{−1c}
Radio luminosity at 1.4 GHz ($L_{1.4GHz}$)	1.07 × 10 ²⁵ W Hz ^{−1f}

^a Jarrett et al. (2000). ^b Jones et al. (2009). ^c This work.

^d Trifalencov (1994). ^e Lauberts & Valentijn (1989).

^f S08.

details) were sourced from the NRAO VLA Archive Survey¹ and re-imaged using *WSCLEAN* (Offringa et al. 2014) version 2.10.0². We employed Briggs weighting with *robust* = +1.0 (Briggs 1995) and used multi-scale clean, with scales between 0 (point sources) and 12× the theoretical beam size, in order to more accurately reconstruct extended radio emission from the jets of ESO 422–G028. Our final VLA image has a representative off-source rms noise of 0.025 mJy beam^{−1}, where the restoring beam is 7.58 × 3.96 arcsec at PA = 18.25°, and a reference frequency of 4.85 GHz.

¹ <http://archive.nrao.edu/nvas/>

² <https://sourceforge.net/p/wsclean/wiki/Home/>

2.1 Environment

ESO 422–G028 is the most massive galaxy in a small group of at least 5 members. The group has a projected diameter of 0.3 Mpc and a low velocity dispersion, indicating it is unvirialised ($\sigma = 83$ km s^{−1}; S08). The small group is located approximately 1.8 Mpc from a large, dense filament of galaxies spanning North-East, which has previously been identified as a supercluster by Kalinkov & Kuneva (1995); the region to the South-West is sparse in comparison. S08 estimate the group is falling towards the supercluster at ~ 600 km s^{−1}.

The pronounced bend in the Northern jet, as well as the strong asymmetry in the two jet lengths, has been attributed to buoyant forces arising from the motion of the group towards the supercluster, as well as higher ambient densities near the large-scale structure (S08). This latter explanation is supported by the excess of soft X-ray sources in the North (Jamroz et al. 2005). Similar phenomena have been observed in other GRGs (Saripalli et al. 1986). S08 also posited that galactic superwinds from AGN in the supercluster may contribute to the asymmetry between the two jets.

3 OBSERVATIONS AND DATA REDUCTION

ESO 422–G028 was observed with the Wide-Field Spectrograph (WiFeS; Dopita et al. 2007, 2010) on the Australian National University 2.3 m telescope at Siding Spring Observatory. WiFeS is an image slicer integral field spectrograph comprising 25 1″-width slices with 0.5″ sampling along the image, binned to 1″ to better match the seeing, providing 1″ × 1″ spatial pixels (*spaxels*) over a 25″ × 38″ field-of-view.

ESO 422–G028 was observed on the 25th and 26th of November 2019 (PI Riseley, proposal ID 4190027) and on the 20th of November 2020 (PI Malik, proposal ID 4200140) using the low-resolution B3000 (3200–5000 Å, $R \sim 3000$, $\Delta v \approx 100$ km s^{−1}) and the high-resolution R7000 (5290–7060 Å, $R \sim 7000$, $\Delta v \approx 40$ km s^{−1}) gratings with the RT560 beam splitter. Three pointings were used to cover the full extent of the galaxy, as shown in Fig. 2. Observations were dithered in ±1″ intervals North-South and East-West to mitigate the effects of bad pixels, each with a 1200 s exposure time for a total effective exposure time of 15600 s. The star HD36702 was used as flux and telluric standard (Bessell 1999).

The observations were reduced in the standard way using *PYWIFES*, the data reduction pipeline for WiFeS (Childress et al. 2014). Cu-Ar and Ne-Ar arc lamp exposures were used to derive the wavelength solution, and exposures of the coronagraphic wire mask were used to calibrate the spatial alignment of the slits. Quartz lamp and twilight flat exposures were used to correct for wavelength and spatial variations in the instrument response respectively. Standard star exposures were used to correct for telluric absorption and for flux calibration. Two data cubes were generated for each exposure, corresponding to the blue (B3000) and red (R7000) arms of the spectrograph respectively.

Sky subtraction was carried out following the method of Zovaro et al. (2020). Regions within the field-of-view with no source signal were used to estimate the sky spectrum, which was then subtracted from each data cube. Sky subtraction residuals were minimised by scaling the flux of the sky spectrum to the measured intensity of a subset of sky lines in each spaxel. The instrumental resolution was estimated from the widths of sky lines to be $\text{FWHM}_{B3000} = 1.4$ Å and $\text{FWHM}_{R7000} = 0.9$ Å in the B3000 and R7000 data cubes respectively.

Mosaics were created by spatially shifting the data cubes by eye

and combining them by taking the sigma-clipped mean of each pixel. 1σ errors for each pixel value in the final mosaic were derived by combining the variance extensions from each individual cube. The mosaicked data cubes were corrected for foreground Galactic extinction assuming $A_V = 0.0454$ from the extinction map of [Schlafly & Finkbeiner \(2011\)](#) and using the reddening curve of [Fitzpatrick & Massa \(2007\)](#) with $R_V = 3.1$.

Fig. 3 shows the spectra from the B3000 and R7000 data cubes extracted from an aperture of radius $1R_e$ centred on ESO 422–G028. The continuum is dominated by deep stellar absorption features, superimposed with strong H α , [N II] and [S II] emission exhibiting complex, asymmetric line profiles. The comparative paucity of the H β and [O III] lines firmly classifies ESO 422–G028 as a low-excitation radio galaxy (LERG; [Best & Heckman 2012](#)).

The pseudo V-band continuum, generated by summing the wavelength slices from 5000–6000 Å, is shown in Fig. 4. The surface brightness profile is smooth; no morphological perturbations are apparent at the modest $1''$ spatial resolution of WiFeS. Also shown are H α and [N II] line profiles extracted from the Eastern, central and Western regions of the galaxy, and a position-velocity (PV) diagram which shows the line profiles extracted from a horizontal slit across the centre of the galaxy. Although regular rotation is apparent in the PV diagram, the line profiles are highly asymmetric and vary dramatically across the galaxy.

Due to the steep surface brightness profile of ESO 422–G028, only a handful of spaxels in the centre of the galaxy have sufficient S/N to reliably determine the properties of the stellar population and emission-line gas. We therefore spatially binned the data cube using a Voronoi tessellation via the PYTHON implementation of VORBIN³ ([Cappellari & Copin 2003](#)). This binning method enforces a minimum S/N ratio in each bin whilst ensuring round, compact bin shapes. To determine the binning, we generated an image and the corresponding variance by summing the B3000 data and variance cubes from 5280–5288 Å, and enforced a minimum S/N of 60. This translated to a median S/N between 10 and 25 per spectral pixel for each bin. Fig. 4 shows the resulting bins. Binned data and variance cubes were generated by simply adding the spectra from each spaxel of the data and variance cubes respectively; these binned cubes were used for the remainder of the analysis.

4 STELLAR POPULATION ANALYSIS

We used the PYTHON implementation of Penalized Pixel Fitting (PPXF; [Cappellari & Emsellem 2004](#); [Cappellari 2017](#))⁴ to analyse the age, metallicity and kinematics of the stellar population in each bin by determining the linear combination of simple stellar population (SSP) templates that best describes the stellar continuum.

In order to fit the stellar continuum across the full wavelength range of our WiFeS observations, we spectrally convolved the R7000 cube with a Gaussian kernel with $\text{FWHM} = \sqrt{\text{FWHM}_{\text{B3000}}^2 - \text{FWHM}_{\text{R7000}}^2}$ before spectrally binning the cube to the resolution of the B3000 cube and merging the cubes together, creating a “combined” data cube.

Visual inspection of the spectra revealed deep NaD absorption (rest-frame wavelengths 5889.9 Å and 5895.9 Å; [Morton 1991](#)).

In some bins, the two lines comprising the doublet are clearly resolved, and are much narrower than that expected from stellar absorption, indicating the absorption is partially interstellar in origin. We therefore carried out our PPXF analysis with this feature masked out to prevent the interstellar absorption biasing the fit. The interstellar NaD absorption is discussed at length in Section 6.

We used the SSP templates of [González Delgado et al. \(2005\)](#) generated from the Padova isochrones with a Salpeter IMF, spanning an age range of approximately 4 Myr to 18 Gyr divided into 75 bins with three metallicities ($0.2Z_\odot$, $0.4Z_\odot$ and $0.95Z_\odot$). These templates were chosen due to their high spectral resolution, meaning we did not need to degrade the spectral resolution of our observations prior to running PPXF. The Padova isochrones were used as they include stellar evolution along the red giant branch, which is important for accurately modelling older stellar populations characteristic of ETGs such as ESO 422–G028, unlike the Geneva isochrones. PPXF was run twice in each bin: a first time in order to determine the best-fit age and metallicity, and a second time to determine the stellar kinematics.

To obtain the best-fit age and metallicity template weights in each bin, the stellar continuum and the emission lines were fitted to the “combined” data cube simultaneously, adopting independent velocity components for each. One kinematic component was adopted for the stars, and two components were used for the emission lines, each modelled by Gaussian profiles. For all kinematic components, only the line-of-sight (LOS) velocity and velocity dispersion were fit. A 4th-order multiplicative polynomial was included in the fit to compensate for extinction and calibration errors. *Regularisation* was used to bias the template weights towards the smoothest solution consistent with the data using the method detailed in [Boardman et al. \(2017\)](#)

We note that the emission lines were only fit during the PPXF fit to ensure accurate fitting of the stellar continuum. We did not use the PPXF fit to *analyse* the gas emission lines: we instead fit these separately after subtraction of the stellar continuum, as detailed in Section 5, in order to achieve greater control over the fitting process required for our analysis.

In all regions, ESO 422–G028 is dominated by old stellar populations; however, bins in the region to the North-West also exhibit a much younger component, with ages ≤ 10 Myr. An example of the stellar fit to one such bin is shown in Fig. 5.

To estimate the total mass of both the old and young stellar populations, we converted the luminosity-weighted template weights into mass-weighted template weights. “Age slices”, shown in Fig. 6, show the total masses associated with stellar templates from the PPXF fit within different age ranges in each bin. The young stellar populations are concentrated in the region to the North-West. The weights and metallicities from all bins were added together to produce the histogram shown in Fig. 6, which essentially shows the star formation history (SFH) of ESO 422–G028. There are two peaks in the SFH: one at ≤ 10 Myr, and another at ≥ 10 Gyr. The total mass of the young stellar population is approximately $10^{7.6} M_\odot$, representing only a minute fraction of the total stellar mass, which is approximately $10^{11.4} M_\odot$.

To confirm the presence of young stellar populations, we re-ran our PPXF fits twice using (1) the Padova isochrones but with 1 kinematic component for the emission lines, and (2) the Geneva isochrones but with 2 kinematic components for the emission lines. In every bin, the best-fit stellar continua and SFHs were very similar regardless of the number of kinematic components or the isochrones used, although our fits using the Geneva isochrones yielded a more metal-rich young stellar population a few Myr older than those predicted from our fits

³ <https://www-astro.physics.ox.ac.uk/~mxc/software/#binning>

⁴ <https://www-astro.physics.ox.ac.uk/~mxc/software/#ppxf>

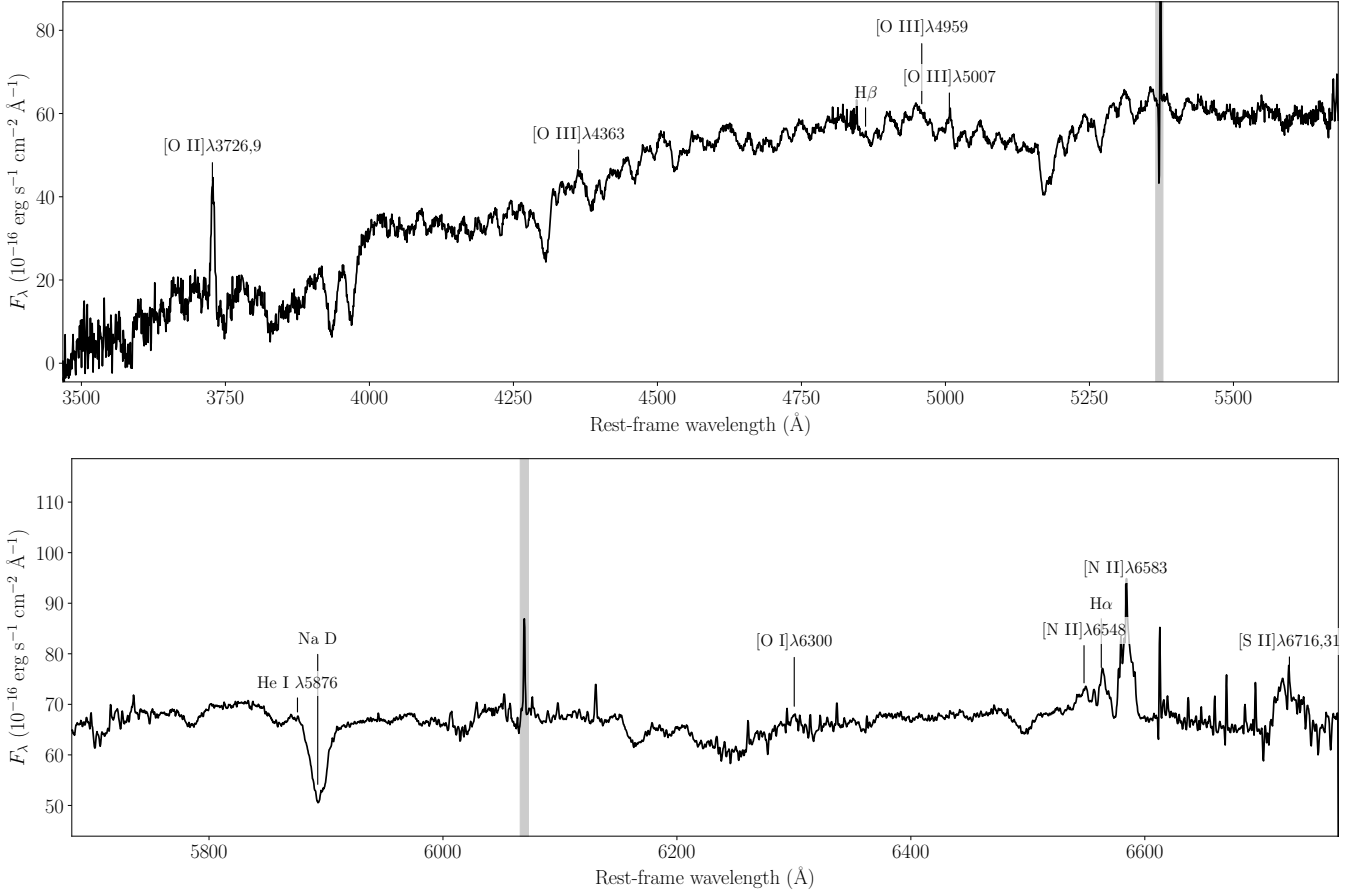


Figure 3. Integrated spectra of ESO 422–G028 from the blue (top) and red (bottom) WiFeS data cubes, extracted from an aperture with radius $1R_e$. The shaded grey regions denote spectral windows dominated by sky line residuals. The R7000 spectrum has been smoothed with a boxcar filter with radius of 3 spectral pixels.

using the Padova isochrones. We therefore do not make any claims as to the precise metallicity or age of the young stellar population, except for that it has an age ≤ 10 Myr.

The stellar kinematics were obtained using a separate PPFIT fit. First, the best-fit emission line profiles obtained from the age and metallicity fit were subtracted from the “combined” data cube. We then ran PPFIT on this cube with an additive 12th-order polynomial. Regularisation was not used in this fit, because it is not required to accurately constrain stellar kinematics. Fig. 7 shows the LOS velocity and velocity dispersion. There is only weak stellar rotation, with velocities peaking at approximately 35 km s^{-1} relative to systemic, whereas the velocity dispersion is broad, reaching values of 330 km s^{-1} in the central regions and decreasing smoothly outwards. Using eqn. 6 of Emsellem et al. (2007) we estimate a spin factor of $\lambda \sim 0.1$, classifying ESO 422–G028 as a slow rotator.

5 EMISSION LINE ANALYSIS

To analyse the emission lines in the binned spectra, an “emission line-only” data cube was first created by subtracting the best-fit stellar continuum in each bin from the binned data cube.

Emission line fluxes were measured by simultaneously fitting the $[\text{O II}]\lambda\lambda 3726, 9\text{\AA}$, $\text{H}\beta\lambda 4861\text{\AA}$, $[\text{O III}]\lambda\lambda 4959, 5007\text{\AA}$, $[\text{O I}]\lambda 6300\text{\AA}$, $\text{H}\alpha\lambda 6563\text{\AA}$, $[\text{N II}]\lambda\lambda 6548, 83\text{\AA}$ and

$[\text{S II}]\lambda\lambda 6716, 31\text{\AA}$ lines using MPPFIT (Markwardt 2009), a PYTHON implementation of the Levenberg-Marquardt algorithm (Moré 1978) developed by M. Rivers⁵. Multiple Gaussian components were fitted, where the number of required components was chosen by eye to account for the total flux of each line. Whilst most bins required one broad and one narrow component to achieve a satisfactory fit, others – generally those with lower S/N – only required a single component. Within each kinematic component, every line was tied to the same radial velocity and velocity dispersion⁶, and the amplitude ratios of the lines in the $[\text{N II}]$ and $[\text{O III}]$ doublets were fixed to 3.06 and 2.94 respectively as dictated by quantum mechanics (Dopita & Sutherland 2003). Rather than fit to the full spectrum, we only fitted to a narrow spectral window around each line in the range $\pm 600 \text{ km s}^{-1}$. In addition to the Gaussian components, a first-order polynomial was fitted within each of these windows to account for residuals due to errors in the stellar continuum fit. Only those bins in which the best fit had a reduced- $\chi^2 < 2$ and $\text{S/N} > 3$ in the total fluxes of both $\text{H}\alpha$ and $\text{H}\beta$ lines were kept.

We note that due to low S/N in the $\text{H}\beta$, $[\text{O III}]$ and $[\text{O I}]$ lines,

⁵ <http://cars9.uchicago.edu/software/python/mpfit.html>.

⁶ Radial velocities were computed from the observed redshift $z_{\text{obs}} = \lambda_{\text{obs}}/\lambda_{\text{rest}} - 1$ using $1 + z_{\text{obs}} = (1 + z_{\text{cos}})(1 + v_{\text{rad}}/c)$.

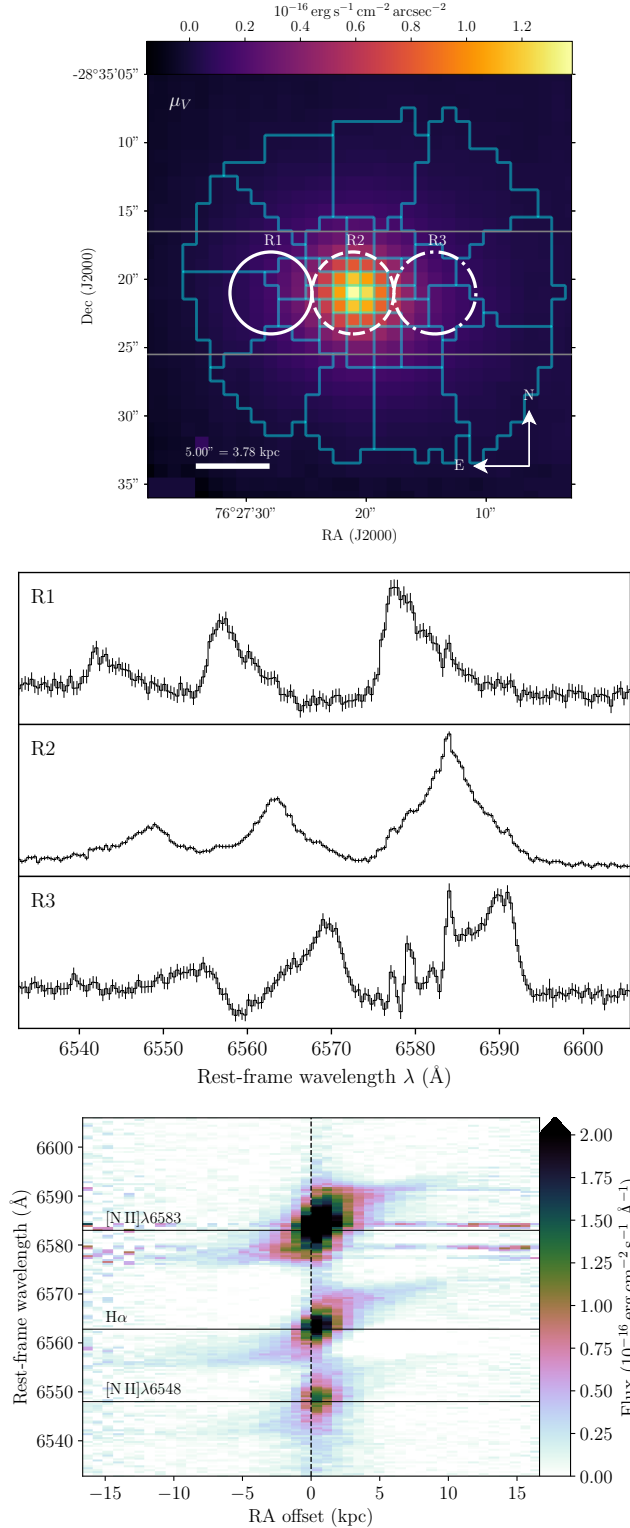


Figure 4. The top panel shows the pseudo V -band continuum generated by summing the WiFeS data cube from 5000–6000 Å, overlaid with the boundaries of the Voronoi bins in cyan. Spectra extracted from the apertures R1, R2 and R3, centred on the $H\alpha$ and $[N II]$ line profiles, are shown in the middle panel, with fluxes scaled arbitrarily. The narrow features visible in the R3 spectrum are skyline residuals. The bottom panel shows a PV diagram running East-West, also centred on the $H\alpha$ and $[N II]$ lines, extracted from the spaxels between the horizontal lines shown in the top panel. Rotation is clearly visible, as are the broad, asymmetric line profiles at larger radii.

Table 2. Total emission line fluxes, corrected for extinction. The quoted uncertainties represent 1σ errors derived from the formal uncertainties of the fits in each bin.

Line	Flux (10^{-15} erg s $^{-1}$ cm $^{-2}$)
$[O II]\lambda\lambda 3726, 9\text{\AA}$	5.2 ± 0.7
$H\beta\lambda 4861\text{\AA}$	7.6 ± 0.7
$[O III]\lambda\lambda 4959, 5007\text{\AA}$	17.0 ± 0.9
$[O I]\lambda 6300\text{\AA}$	4.5 ± 0.3
$H\alpha\lambda 6563\text{\AA}$	20.7 ± 0.5
$[N II]\lambda\lambda 6548, 83\text{\AA}$	38.2 ± 0.8
$[S II]\lambda 6716\text{\AA}$	18.3 ± 0.5
$[S II]\lambda 6731\text{\AA}$	10.2 ± 0.4

the fluxes from the individual kinematic components are unreliable; however, care was taken during the fit to ensure the combined broad and narrow components accurately described the total emission line flux. This fitting process was only used to estimate total fluxes; we fit to the higher-S/N $H\alpha$ and $[N II]$ lines separately to more accurately determine the gas kinematics (see Section 5.3).

Table 2 shows the total emission line fluxes across all bins, corrected for extinction (see Section 5.1).

5.1 Extinction

A_V was computed in each bin from the total $H\alpha$ and $H\beta$ emission line fluxes using the reddening curve of Fitzpatrick & Massa (2007) with $R_V = 3.1$ and assuming an intrinsic $H\alpha/H\beta$ flux ratio of 2.86 (Dopita & Sutherland 2003). A_V was only computed in those bins in which the S/N of the $H\alpha/H\beta$ ratio exceeded 3.

As shown in Fig. 8, there is little extinction in the North-Western regions of the galaxy, whereas A_V reaches values of ~ 1 mag in the South-East. Bins with $A_V < 0$ by more than 1σ are most likely due to systematic errors in the stellar continuum fit. There may be additional systematic errors due to our calculation of A_V using the summed $H\alpha$ and $H\beta$ fluxes from both broad and narrow components, which is problematic if the broad and narrow kinematic components have different intrinsic A_V values. Our assumption of the intrinsic $H\alpha/H\beta$ flux ratio of 2.86 may also not hold, which may be the case if the power source is AGN photoionisation or shocks (see Section 5.2; Dopita & Sutherland 2003). Emission line fluxes were only corrected for extinction in bins in which $A_V > 0$.

5.2 Emission line ratios

To investigate the source of the line emission, we used an optical diagnostic diagram (ODD; Baldwin et al. 1981; Veilleux & Osterbrock 1987) in which the ratios of pairs of emission lines are used to determine the excitation mechanism of the ionised gas. Due to the faintness of the bluer lines, we were unable to analyse the excitation mechanisms of each kinematic component separately; we therefore analysed the total fluxes summed from both broad and narrow components in each bin, as shown in Fig. 9, where each point has been coloured by the velocity dispersion of the broad component, which dominates the flux in most bins. As is typical for a LERG such as ESO 422–G028, the emission line ratios in all bins lie firmly in the Low-Ionisation Emission Region (LIER) quadrant, indicating ionisation dominated either by old stellar populations (Binette et al. 1994; Singh et al. 2013; Belfiore et al. 2016), a low-luminosity AGN (Kauffmann et al. 2003b) or shocks (Allen et al. 2008; Dopita & Sutherland 2017; Sutherland & Dopita 2017).

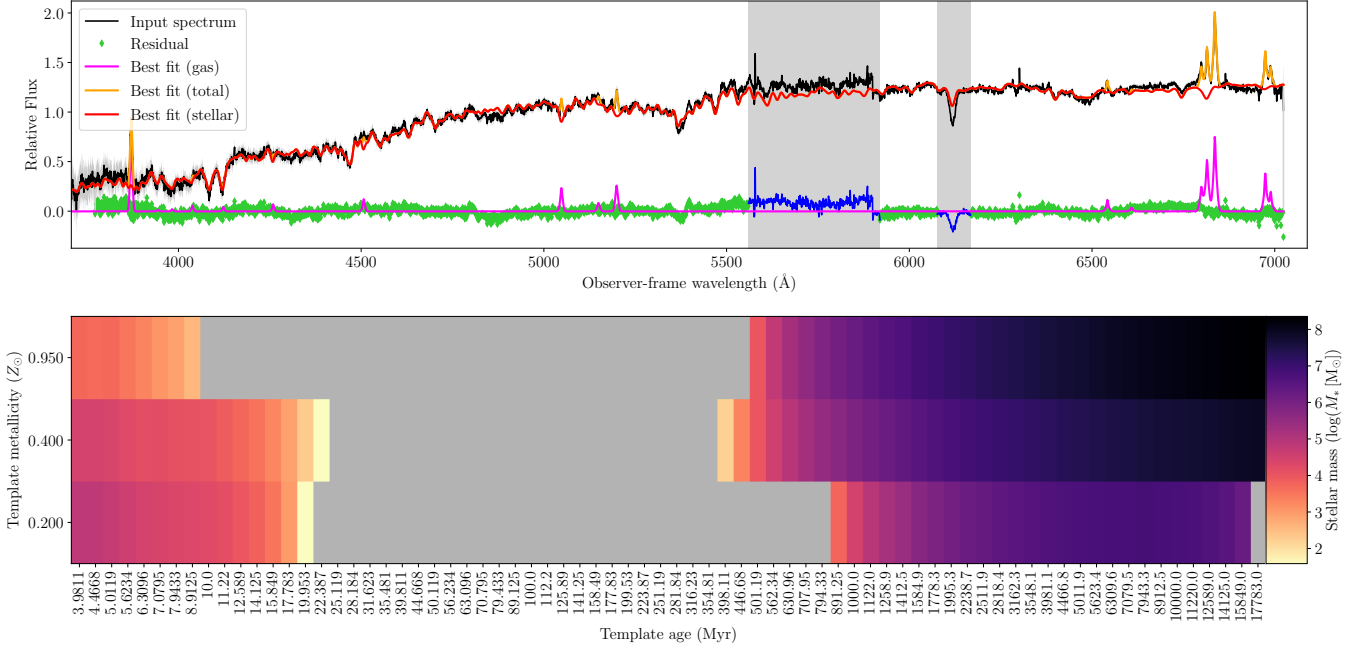


Figure 5. An example stellar continuum fit from one of the Voronoi bins. The upper plot shows the spectrum overlaid with the best-fit stellar continuum computed using `ppxf`; shaded regions in the spectrum denote regions masked out during the fit. The lower plot shows the corresponding mass-weighted stellar template weights, where the grey cells denote templates with a weight of zero.

5.3 Kinematics

To analyse the emission line kinematics, we carried out a separate line fitting procedure for the H α and [N II] lines in the R7000 cubes in order to take advantage of the higher spectral resolution. To create the emission line-only spectra for each bin in the R7000 data cube, we used a cubic spline technique to spectrally interpolate the stellar continuum from the `ppxf` fit to the spectral resolution of the R7000 data cube. The interpolated stellar continua were then subtracted from the spectrum in each bin. The fit was then carried out using the same method described in Section 5.

In most bins, one broad and one narrow component were required to adequately describe the line profiles. In bins where there were multiple fits with differing kinematics but similar reduced- χ^2 values, the fit that would produce the smoothest variation in kinematics across neighbouring bins was chosen. The surface brightness of the H α line in each component is shown in Fig. 10; the broad component is significantly brighter than the narrow component, which appears to increase slightly to the West.

The radial velocity and velocity dispersion of each component is shown in Fig. 11. Also shown is the difference between the stellar and gas velocities for each component. Ordered rotation is apparent in both the broad and narrow components, although the rotation curve of the narrow component is much steeper than that of the broad component. The rotation curves of both components are also much steeper than that of the stars: whilst the stellar velocities peak at 35 km s⁻¹, the broad and narrow components reach maximum radial velocities of approximately 100 km s⁻¹ and 320 km s⁻¹ respectively. The velocity dispersions of the two components also differ vastly: whilst that of the broad component rises smoothly towards the centre, peaking at approximately 225 km s⁻¹, the width of the narrow component remains relatively constant at approximately 60 km s⁻¹ across the entire galaxy.

The starkly different rotation curves of the broad and narrow components, combined with their respective widths, suggests that each component traces a distinct disk. Similar asymmetric line profiles observed in so-called “red geysers” galaxies have recently been attributed to AGN-driven biconical outflows (Roy et al. 2021b). Indeed, ESO 422–G028 shares many properties of red geysers, intermediate-mass ($M_* \sim 10^{10.5} M_\odot$) spheroidal galaxies characterised by low star formation rates and misaligned gas and stellar kinematics (Cheung et al. 2016). However, were the asymmetric line profiles in ESO 422–G028 a result of biconical outflows, this would imply that the conical structures are perpendicular to the kpc-scale jets (see Fig. 2), which would be difficult to explain were the outflows driven by the central AGN. We therefore favour the multiple disk interpretation, although our ability to carry out detailed kinematic modelling is hampered by low S/N and the correspondingly large bins in the outermost regions.

5.4 Star formation rate

The star formation rate (SFR) was first estimated using the SFH obtained from our stellar population analysis (Section 4). As shown in Fig. 6, stellar populations less than 100 Myr old account for approximately $10^{7.6} M_\odot$, corresponding to a mean SFR of $0.4 M_\odot \text{ yr}^{-1}$.

We also estimated the SFR using the H α calibration of Calzetti (2013), $\text{SFR}(\text{H}\alpha) = 5.5 \times 10^{42} L_{\text{H}\alpha} M_\odot \text{ yr}^{-1}$, assuming a Kroupa IMF and a constant SFR over a timescale $\tau \geq 6 \text{ Myr}$. The total extinction-corrected H α luminosity, comprising both broad and narrow components, yields $\text{SFR}(\text{H}\alpha) = 0.39 \pm 0.01 M_\odot \text{ yr}^{-1}$. As shown in Fig. 9, the emission line ratios are LIER-like, indicating the H α emission is dominated by processes other than star formation; this SFR estimate therefore represents an upper limit, although we note that it is consistent with the SFR estimate based on our `ppxf` analysis. The corresponding specific SFR, i.e., the star forma-

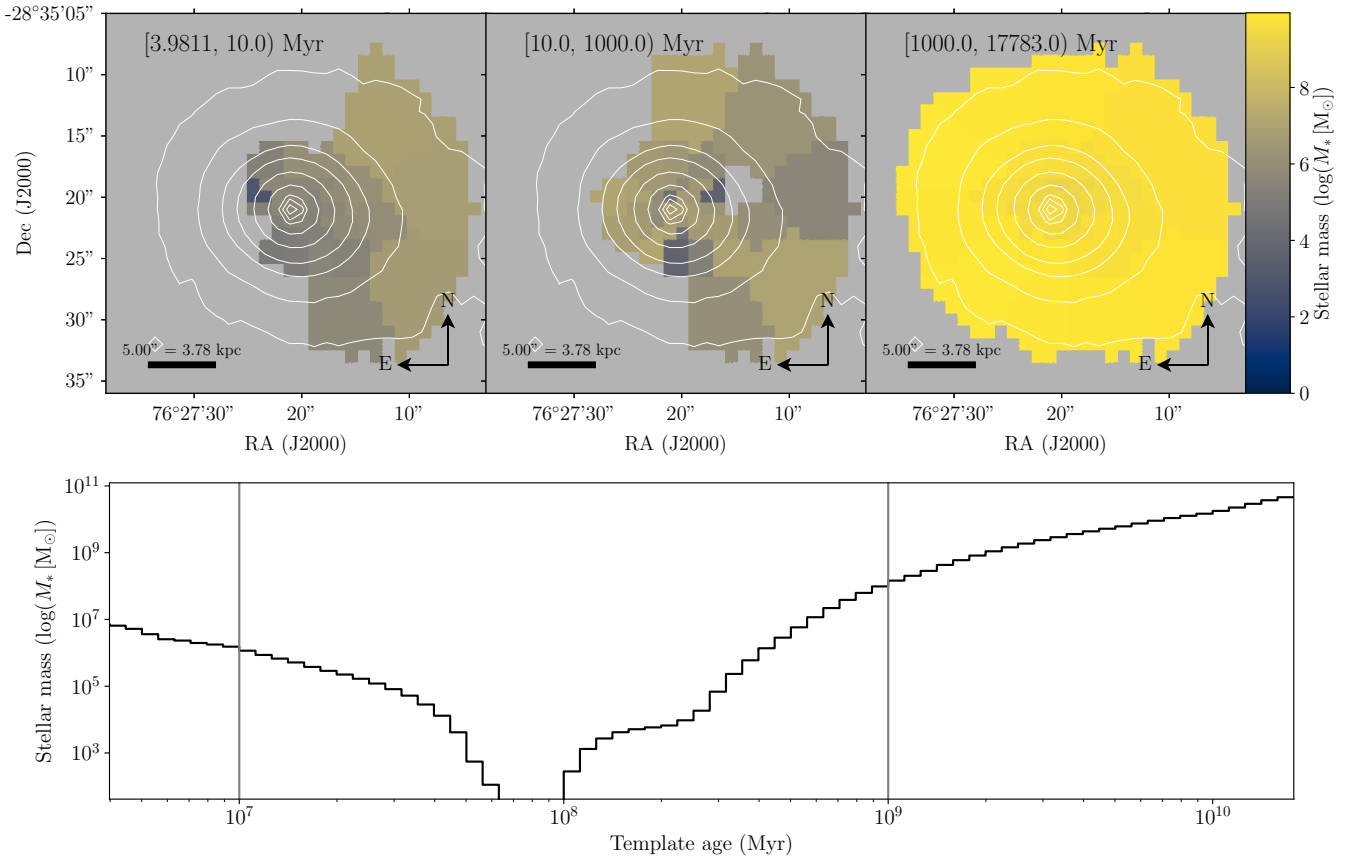


Figure 6. The stellar mass distribution from the ppxf fit in each bin (top), divided into the age ranges indicated in the upper left corner. The contours represent the V-band continuum, with levels 2.5×10^{-18} , 1×10^{-17} , 2×10^{-17} , 3×10^{-17} , 5×10^{-17} , 8×10^{-17} , 1.1×10^{-16} , 1.2×10^{-16} and 1.3×10^{-16} $\text{erg s}^{-1} \text{cm}^{-2} \text{arcsec}^{-2}$. The bottom panel shows the SFH of ESO 422–G028 integrated over all bins and template metallicities. The grey vertical lines show the cuts used to make the stellar mass maps in the upper panel.

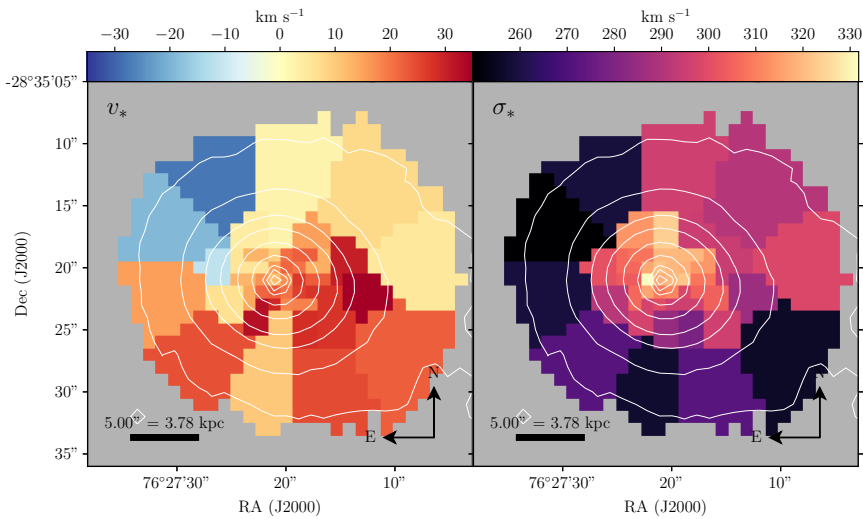


Figure 7. Stellar velocity, relative to systemic (left) and velocity dispersion (right) from the ppxf fit. The contours are as in Fig. 6.

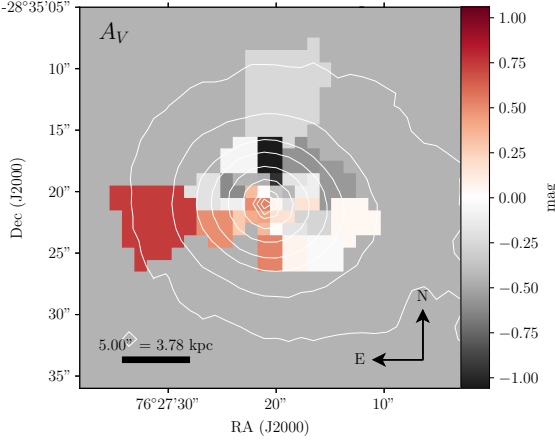


Figure 8. Total extinction in the V-band, A_V , calculated from the total H α and H β emission line fluxes. Negative values are probably a result of errors in the stellar continuum fit. The contours are as in Fig. 6.

tion rate per unit stellar mass, of ESO 422–G028 is approximately $\text{sSFR} \sim 0.001 \text{ Gyr}^{-1}$.

5.5 Eddington ratio

Here we compute the Eddington ratio

$$\lambda_{\text{Edd}} = \frac{L_{\text{bol}}}{L_{\text{Edd}}} \quad (1)$$

where L_{bol} is the bolometric luminosity of the AGN and L_{Edd} is the Eddington ratio. To compute L_{bol} we use the relation of Heckman et al. (2004)

$$L_{\text{bol}} = 3500 L_{[\text{O III}] \lambda 5007} \text{ erg s}^{-1} \quad (2)$$

where $L_{[\text{O III}] \lambda 5007}$ is the luminosity of the $[\text{O III}] \lambda 5007 \text{ \AA}$ line. Using the integrated fluxes shown in Table 2 we find $L_{[\text{O III}] \lambda 5007} = (4.3 \pm 0.2) \times 10^{40} \text{ erg s}^{-1}$, corresponding to $L_{\text{bol}} = (1.50 \pm 0.08) \times 10^{44} \text{ erg s}^{-1}$.

The Eddington luminosity is given by

$$L_{\text{Edd}} = 1.3 \times 10^{38} \left(\frac{M_{\text{BH}}}{M_{\odot}} \right) \text{ erg s}^{-1} \quad (3)$$

To estimate the supermassive black hole mass M_{BH} we use the $M_{\text{BH}} - \sigma_*$ relation (Ferrarese & Merritt 2000; Gebhardt et al. 2000; Kormendy & Ho 2013)

$$\frac{M_{\text{BH}}}{10^9 M_{\odot}} = \left(0.310^{+0.037}_{-0.033} \right) \left(\frac{\sigma_*}{200 \text{ km s}^{-1}} \right)^{4.38 \pm 0.29} \quad (4)$$

where σ_* is the stellar velocity dispersion within $1R_e$. To compute σ_* we used PPFIT to fit the stellar continuum to the spectrum extracted from an aperture with radius $1R_e = 12.56''$ and an axis ratio of 1.25 (Lauberts & Valentijn 1989). We find $\sigma_* = 293 \text{ km s}^{-1}$, which gives $M_{\text{BH}} = 1.7^{+0.4}_{-0.3} \times 10^9 M_{\odot}$ and a corresponding Eddington luminosity $L_{\text{Edd}} = 2.2^{+0.5}_{-0.4} \times 10^{47} \text{ erg s}^{-1}$.

Substituting these values into Eqn. 1 gives $\lambda_{\text{Edd}} = (6 \pm 2) \times 10^{-4}$, suggesting radiatively inefficient accretion as is characteristic of LERGs (Best & Heckman 2012). Both the Eddington ratio and BH mass of ESO 422–G028 are also characteristic of the sample of low-excitation GRGs studied by Dabhade et al. (2020b).

The mass accretion rate required to power the AGN can be estimated using

$$\dot{M} = \frac{L_{\text{bol}}}{c^2 \eta} \quad (5)$$

where $\eta \approx 0.1$ is the efficiency (Riffel et al. 2008); adopting $L_{\text{bol}} \sim 10^{44} \text{ erg s}^{-1}$ gives $\dot{M} \sim 10^{-2} M_{\odot} \text{ yr}^{-1}$.

6 NA D ABSORPTION LINE ANALYSIS

As illustrated in Fig. 5, the best-fit stellar continua in most bins significantly under-estimates the strength of the Na D absorption, suggesting this feature is partially interstellar in origin. With an ionisation potential of 5.1 eV, interstellar Na D absorption is a tracer of neutral gas.

To further investigate these residuals, we normalised the spectra in each bin of the R7000 cube by the stellar continuum as follows. In each bin, the stellar continuum from the PPFIT fit was spectrally interpolated using a cubic spline technique to the spectral resolution of the R7000 data cube. The spectrum was then divided by the interpolated stellar continuum.

The residual absorption profiles in each bin are shown in Fig. 12. A variety of profile shapes are present: in some bins, the lines of the doublet are clearly visible, whereas in others they are unresolved. In many bins, the profiles are noticeably asymmetric, exhibiting clear broad and narrow kinematic components. The overall absorption strength increases smoothly from South-East to North-West; interestingly, the deepest Na D residuals are found in regions with $A_V \sim 0$ (Fig. 8), whereas the regions with greater extinction exhibit little to no interstellar Na D absorption. In most galaxies, interstellar Na D absorption is correlated with A_V due to dust in the absorbing gas (e.g., Rupke et al. 2021; Cheung et al. 2016).

We used the analytical expressions for Na D absorption profiles given by Rupke et al. (2005a) to fit the residual Na D absorption features in each bin, where we assumed a Maxwellian velocity distribution for the absorbing gas, and a covering fraction C_f that does not vary with wavelength. For each kinematic component, the two lines in the doublet were modelled assuming the ‘‘completely overlapping’’ case, such that the intensity $I(\lambda)$ of the absorption, assuming an incident continuum level of unity, is given by

$$I(\lambda) = 1 - C_f + C_f e^{-\tau_b(\lambda) - \tau_r(\lambda)} \quad (6)$$

where $\tau_b(\lambda)$ and $\tau_r(\lambda)$ are the optical depths of the blue and red lines in the doublet (at $\lambda_b = 5889.9 \text{ \AA}$ and $\lambda_r = 5895.9 \text{ \AA}$ in air respectively; Morton 1991). Under the assumption of a Maxwellian velocity distribution, the optical depth of line i centred at wavelength λ_i is a Gaussian of the form

$$\tau_i(\lambda) = \tau_{i,0} \exp \left[\frac{-(\lambda - \lambda_i)^2}{(\lambda_i b/c)^2} \right] \quad (7)$$

where $\tau_{i,0}$ is the ‘‘central’’ optical depth at $\lambda = \lambda_i$, c is the speed of light and b is the Doppler line width, related to the Gaussian σ via $\sigma = b/\sqrt{2}$. We assumed $\tau_{b,0} = 2\tau_{r,0}$ (Morton 1991).

Two kinematic components were fitted to the absorption profiles, combining each component $I_1(\lambda)$ and $I_2(\lambda)$ (each consisting of the two lines in the doublet) assuming the ‘‘partial overlap’’ case of Rupke et al. (2005a), in which case the residual absorption profile is given by

$$I(\lambda) = I_1(\lambda)I_2(\lambda). \quad (8)$$

At widths $b \gtrsim 300 \text{ km s}^{-1}$ the two lines in the doublet become unresolved, and the line shape approaches a Gaussian or Voigt-like profile. In this regime, it becomes difficult to estimate both C_f and τ_0 : within the measurement uncertainties of our data, an absorber with large covering fraction and low optical depth may become indistinguishable from one with low covering fraction and high optical

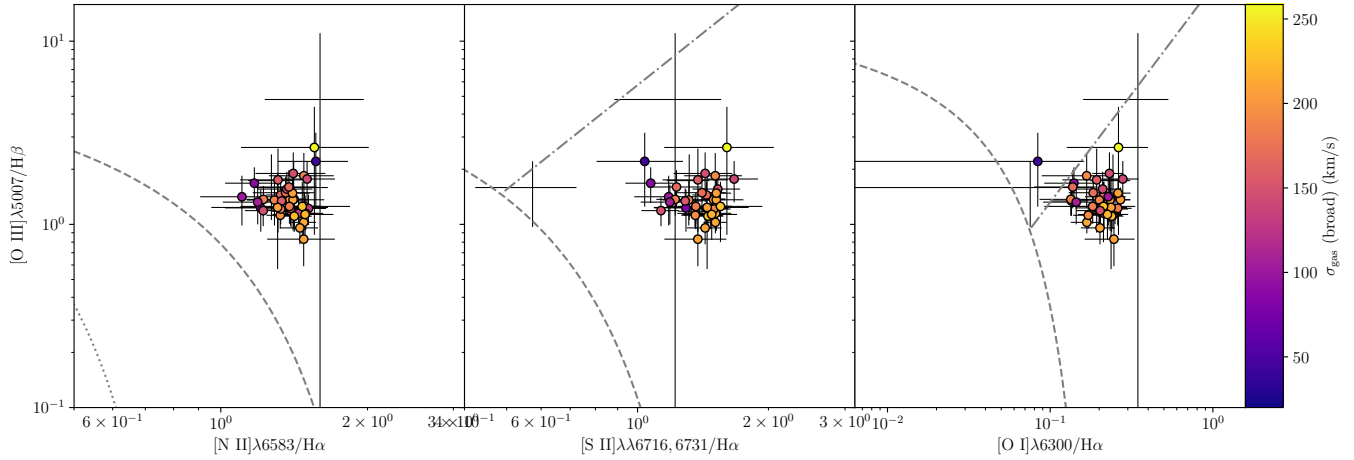


Figure 9. Optical diagnostic diagram (ODD; Baldwin et al. 1981; Veilleux & Osterbrock 1987) where the line ratios have been computed from the *total* (narrow plus broad) line fluxes in each bin, coloured by the velocity dispersion of the broad component. The grey dashed lines represent the maximum $[\text{O III}]/\text{H}\beta$ ratio that can arise from star formation alone, derived from photoionisation models (Kewley et al. 2001). In the left panels, the dotted line is the equivalent empirical relation of Kauffmann et al. (2003a) which separates star-forming galaxies and AGN hosts. In the middle and right panels, the dot-dashed lines of Kewley et al. (2006) separate Seyfert-like (above) and LIER-like ratios (below the line).

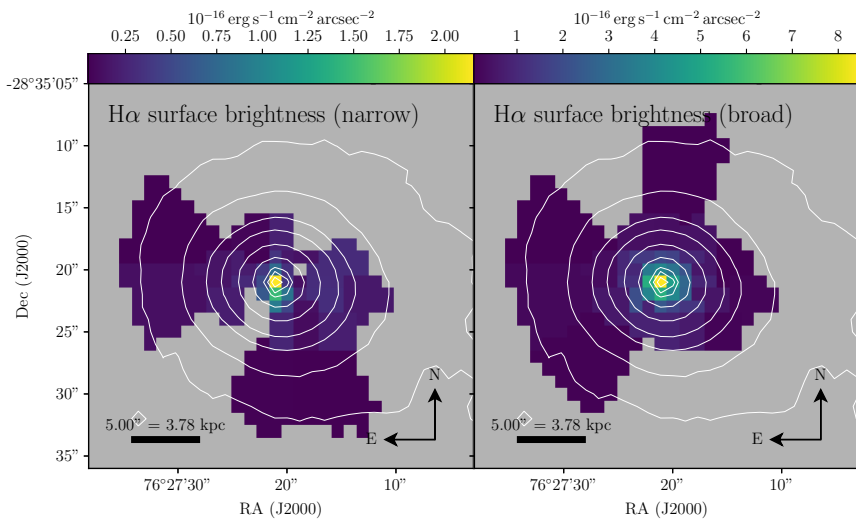


Figure 10. $\text{H}\alpha$ surface brightness of the narrow (left) and broad (right) kinematic components. The contours are as in Fig. 6.

depth. In these cases, C_f and τ_0 become strongly degenerate, and the formal uncertainties provided by simple least-squares minimisation techniques are inaccurate as they do not reflect this anticorrelation.

We instead opted to use a Bayesian parameter estimation technique to fit the line profiles in each bin, as these approaches numerically estimate the posterior probability distribution functions (PDFs) of the model parameters given the data, enabling correlations between parameters to be easily visualised and interpreted. We used *nested sampling* (Skilling 2004; Skilling 2006) to compute the PDFs of the model parameters Θ given the data \mathbf{D} and the model M . Other Bayesian parameter estimation techniques, such as Monte-Carlo Markov Chain and dynamical nested sampling, have also been used to fit Na D absorption profiles in the past (e.g., Sato et al. 2009; Roy et al. 2021a).

The posterior $\mathbf{P}(\Theta|\mathbf{D}, M)$ is given by Bayes’ theorem,

$$\mathbf{P}(\Theta|\mathbf{D}, M) = \frac{\mathbf{P}(\mathbf{D}|\Theta, M) \mathbf{P}(\Theta|M)}{\mathbf{P}(\mathbf{D}|M)} \quad (9)$$

where $\mathbf{P}(\mathbf{D}|\Theta, M)$ is the *likelihood* of observing the data given the parameters and the model, and $\mathbf{P}(\Theta|M)$ is the *prior* probability distribution of the model parameters. $\mathbf{P}(\mathbf{D}|M)$ is the *Bayesian evidence*, or the likelihood of the data given the model, which is the integral of the likelihood and the prior over all parameter space:

$$\mathbf{P}(\mathbf{D}|M) = \int_{\Omega_{\Theta}} \mathbf{P}(\mathbf{D}|\Theta, M) \mathbf{P}(\Theta|M) d\Theta \quad (10)$$

Nested sampling produces an estimate of $\mathbf{P}(\mathbf{D}|M)$ by approximating the integral in Eqn. 10 via computing “iso-likelihood” surfaces in parameter space Ω_{Θ} . The likelihood and the prior at the sampled

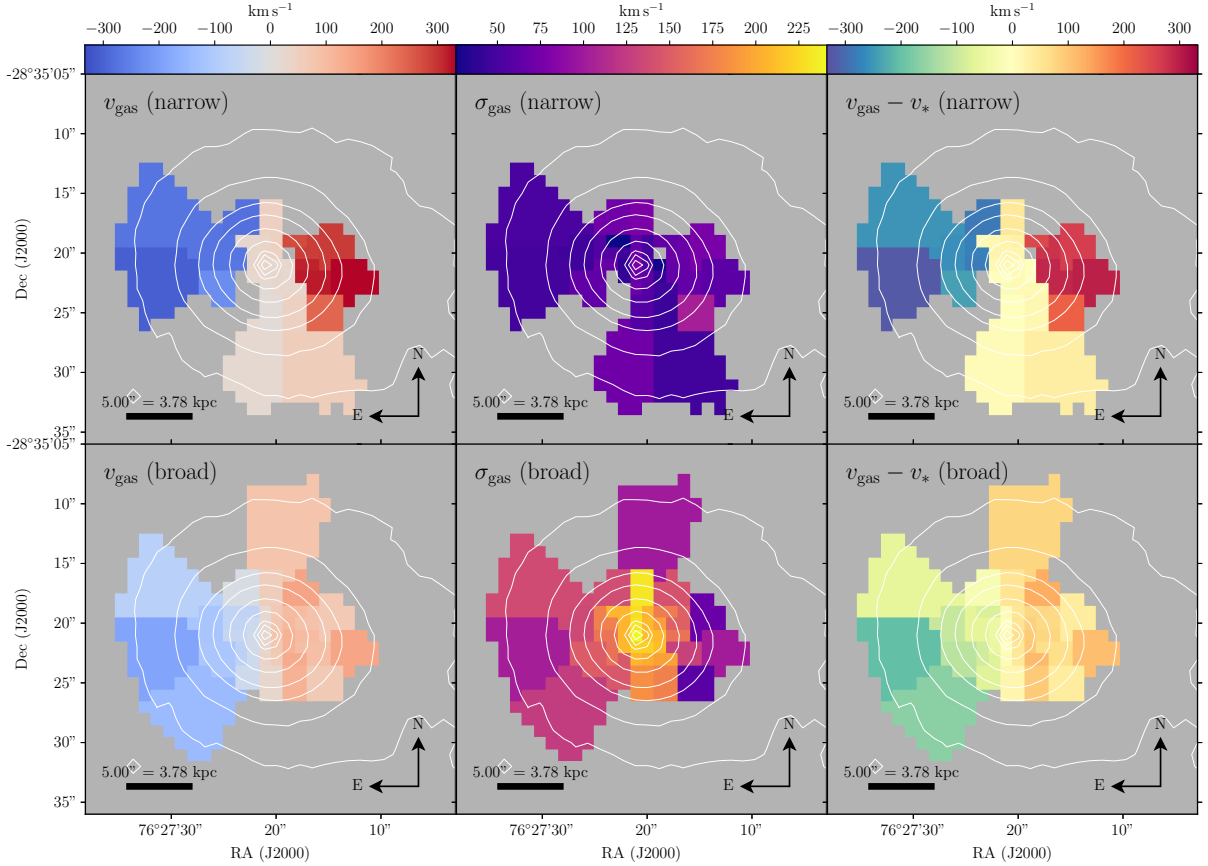


Figure 11. Ionised gas radial velocity, relative to systemic (left), gas velocity dispersion (Gaussian σ , minus instrumental dispersion, right) and gas velocity relative to the stellar velocity (centre) of the narrow (top row) and broad (bottom row) emission line components in each bin. The contours are as in Fig. 6.

points in parameter space are also evaluated as part of this computation, enabling the posterior to be sampled as per Eqn. 9. In this way, nested sampling can be used to approximate the posterior PDFs of model parameters.

To estimate posterior probability distributions and the Bayesian evidence for our models, we used the nested sampling Monte Carlo algorithm MLFRIENDS (Buchner 2014, 2019) implemented in the PYTHON package ULTRANEST⁷ (Buchner 2021).

In each bin, we estimated the posterior PDF for absorption profile models comprising both one and two kinematic components, where the best-fit number of components in each bin was determined by eye. We did not convolve the model profiles with the instrumental resolution as this greatly increased the computational time, and is expected to have only a modest impact on the results (Rupke et al. 2005a). The reported best-fit parameter values, and corresponding upper and lower error estimates, for each component were computed from the quartiles of the samples in the marginalised PDFs.

We adopted uniform priors for our model parameters. The covering fraction was limited to $C_f \in [0, 1]$, and the optical depth was limited to $\tau_0 \in [0, 5]$ because the lines saturate at optical depths $\tau_0 \geq 5$. The radial velocity was constrained to $v \in [-100, 500]$ km s⁻¹ relative to systemic. For two-component fits, we fitted a narrow and a broad component by defining priors $b_{\text{narrow}} \in [10, 200]$ km s⁻¹ and $b_{\text{broad}} \in [200, 800]$ km s⁻¹. For single component fits we set $b \in [10, 800]$ km s⁻¹.

⁷ <https://johannesbuchner.github.io/UltraNest/>

Examples of the best-fit line profiles and corresponding corner plots for two bins are given in Appendix A. The marginalised posterior PDFs for both C_f and τ_0 tend to have long tails extending to large values, resulting in significantly asymmetric upper and lower error estimates. Strong correlations between C_f and τ_0 are also present in most bins. In bins where two components were required, the PDFs corresponding to the parameters of the narrow component tend to be well-defined and quasi-Gaussian (Fig. A2) whereas the PDFs for the broad component parameters tend to be irregular and even multi-modal (Fig. A3), reflecting the difficulties in constraining model parameters when the two lines become blended.

Fig. 13 shows the 50th percentile τ_0 and C_f values in each bin. The narrow component is optically thick, with $\tau_0 \geq 1$ in most bins, but with low covering fractions, suggesting this component traces dense clumps. Meanwhile, the broad component is optically thin ($\tau_0 \lesssim 1$) with similarly low covering fractions.

As shown in Fig. 14, both narrow and broad components are redshifted by up to +250 km s⁻¹ with respect to systemic velocity. Importantly, because the Na D lines are viewed in absorption against the stellar continuum, this indicates the absorption traces *inflowing* material. The narrow component is characterised by velocity dispersions of 60–100 km s⁻¹ and exhibits a velocity shear similar to that of the ionised gas, suggesting this gas traces the same rotating structure (see Fig. 11). In contrast, the broad component shows no clear signs of rotation, and is very broad, with $\sigma \geq 500$ km s⁻¹ in some bins.

Also shown in Fig. 14 is the difference between the stellar and Na D radial velocities. To determine whether the absorption is sufficiently

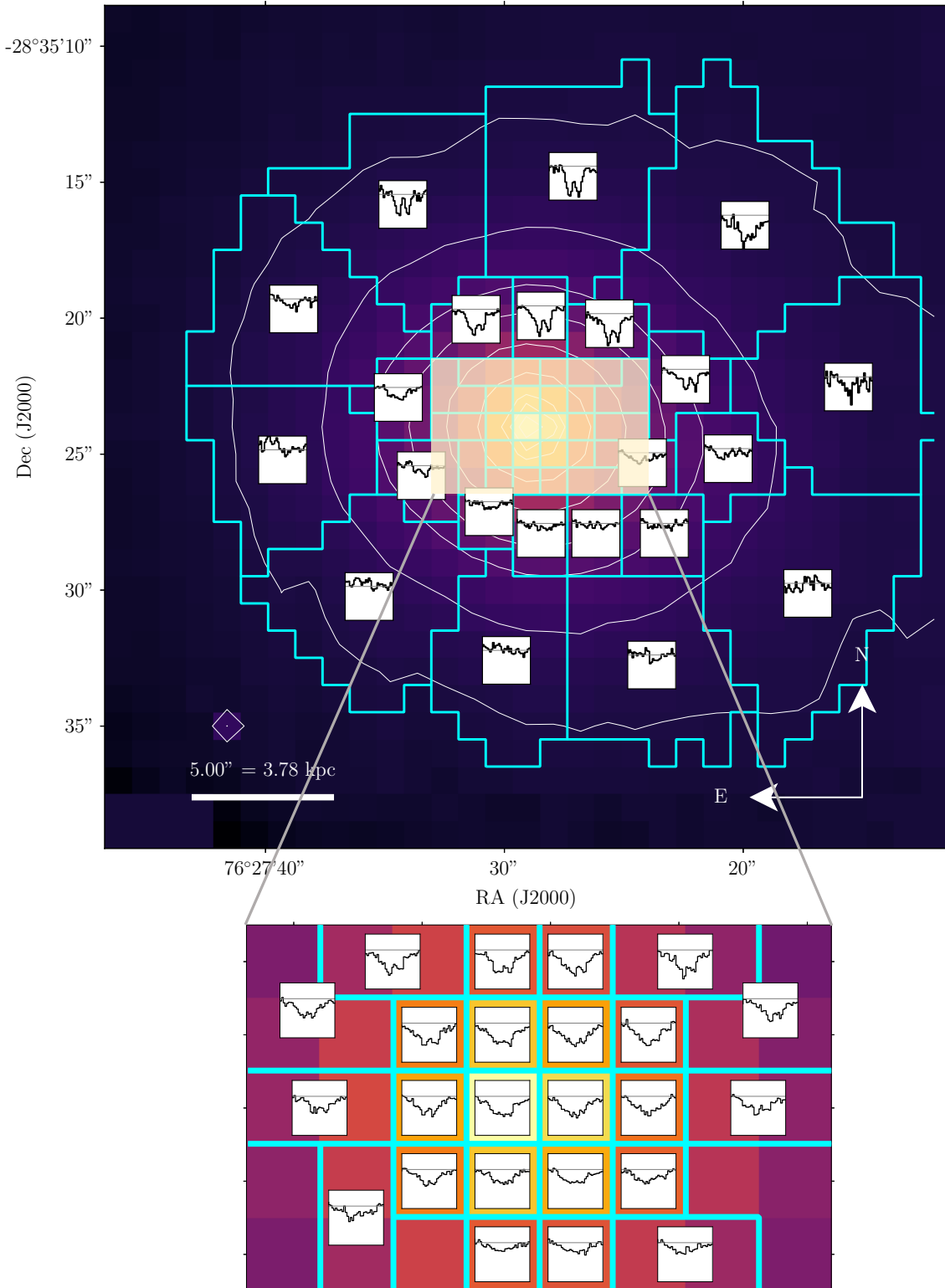


Figure 12. The residual Na D absorption profile in each bin (denoted by the cyan outlines), overlaid on the V-band continuum. The lower plot shows an enlarged view of the central region. Each inset set of axes has the same scaling on the x- and y-axes. The grey horizontal line denotes $F_{\lambda}/F_{*,\lambda} = 1.0$. The contours are as in Fig. 6.

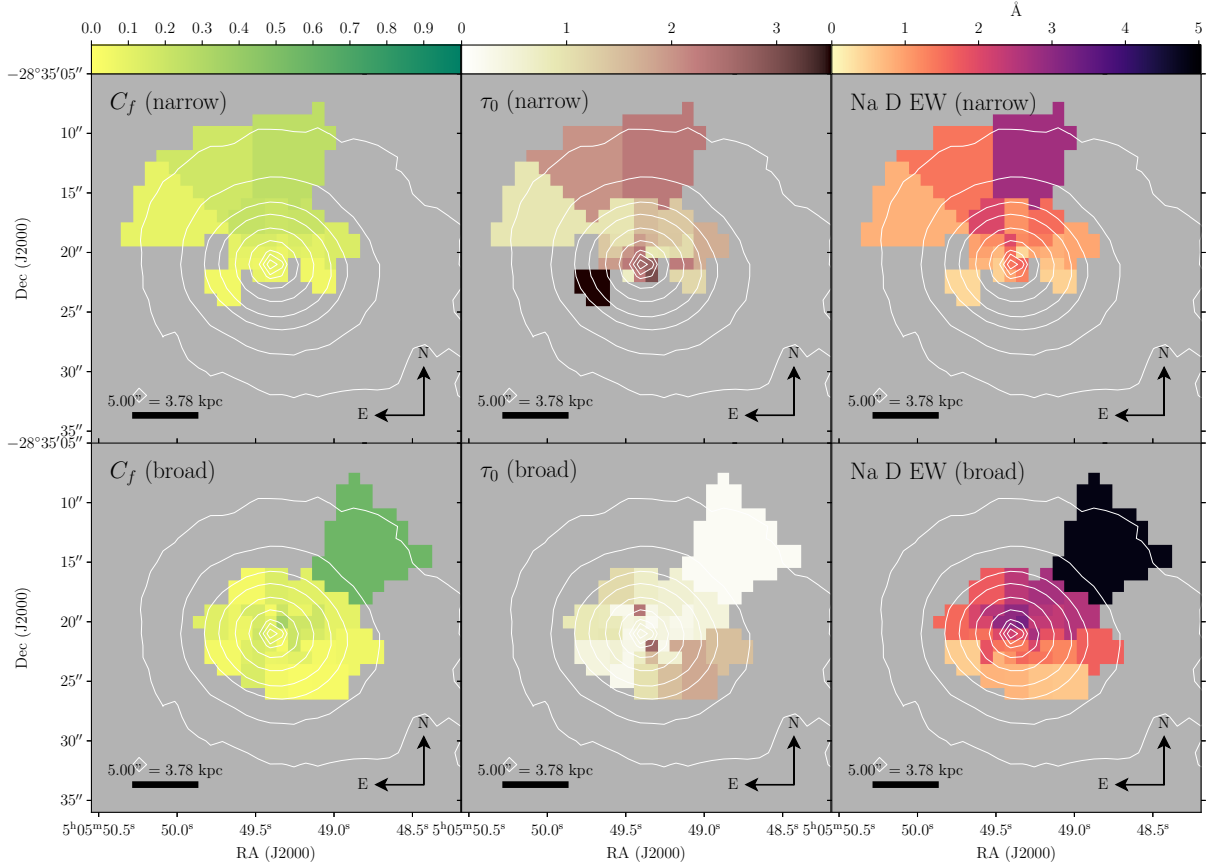


Figure 13. Covering fraction C_f (left), central optical depth τ_0 of the Na D red line (centre) and EW (right) of the best-fit narrow (top row) and broad (bottom) kinematic components. The contours are as in Fig. 6.

redshifted to represent an inflow, we adopted the $2\sigma_{\text{v}_{\text{NaD}}}$ criterion of Krug et al. (2010) where $\sigma_{\text{v}_{\text{NaD}}}$ is the lower error on the LOS Na D velocity. For the narrow component, the interstellar Na D meets this requirement in most bins. The offset of the broad component does not exceed the 2σ criterion in roughly half of the bins, although this is likely a result of the larger uncertainty on the fitted velocity due to the broadness of the profile.

Fig. 13 shows the rest-frame equivalent width (EW) calculated from the best-fit $I(\lambda)$ in each bin, using

$$\text{EW}_{\text{tot}} = \frac{1}{1+z} \sum_i \left\{ \int_0^\infty [1 - I_{b,i}(\lambda)] d\lambda + \int_0^\infty [1 - I_{r,i}(\lambda)] d\lambda \right\} \quad (11)$$

where $I_{b,i}(\lambda) = 1 - C_{f,i} + C_{f,i}e^{-\tau_{b,i}(\lambda)}$ and $I_{r,i}(\lambda) = 1 - C_{f,i} + C_{f,i}e^{-\tau_{r,i}(\lambda)}$ are the red and blue components of the doublet in each kinematic component i . The EW ranges from 1–5 Å and increases smoothly from South-East to North-West, suggesting that the gas is inflowing from the North. Interestingly, the EWs are significantly higher than those observed in a sample of local active and inactive galaxies with Na D inflows reported by Roberts-Borsani & Saintonge (2019), who detected EWs of $\lesssim 1.3$ Å, and our measured EWs are among the highest of those detected in red geysers galaxies (Roy et al. 2021a). The EWs are more similar to those observed in the sample of ultra-luminous infrared galaxies (ULIRGs) by Rupke et al. (2005b) (0–10 Å), all of which host outflows.

In addition to interstellar absorption, stellar template mismatch has been observed to cause significant Na D residuals in early-type

galaxies. The mismatch is thought to result from elevated Na abundances arising from non-solar abundance scalings, and leaves broad, residual absorption features centred at the systemic stellar velocity (Jeong et al. 2013; Park et al. 2015). In ESO 422–G028, the narrow component is clearly interstellar in origin, as evidenced by its low velocity dispersion ($\sigma_{\text{NaD}} \lesssim 100 \text{ km s}^{-1}$) compared to that of the stellar component ($\sigma_* \gtrsim 250 \text{ km s}^{-1}$; see Fig. 7). The broad component, on the other hand, has velocity dispersions similar to that of the stars (Fig. 7); however, both the velocity dispersion and the EW of the broad component increase markedly from South to North. In fact, inspection of Fig. 12 reveals negligible residual absorption – broad or narrow – in the Southern regions of the galaxy, indicating the broad component is predominantly interstellar in origin, although some contamination from residual stellar absorption may be present. We therefore repeated our analysis, substituting a stellar component, that was fixed to the stellar velocity and velocity dispersion, for the broad interstellar component. As detailed in Appendix B, the resulting amplitude of the stellar component varies significantly across the galaxy, confirming that the broad component is predominantly interstellar.

6.1 Mass inflow rate

To estimate the mass inflow rate, we used the method described by Rupke et al. (2005a). We note that this method was originally developed to estimate mass outflow rates, although the same technique

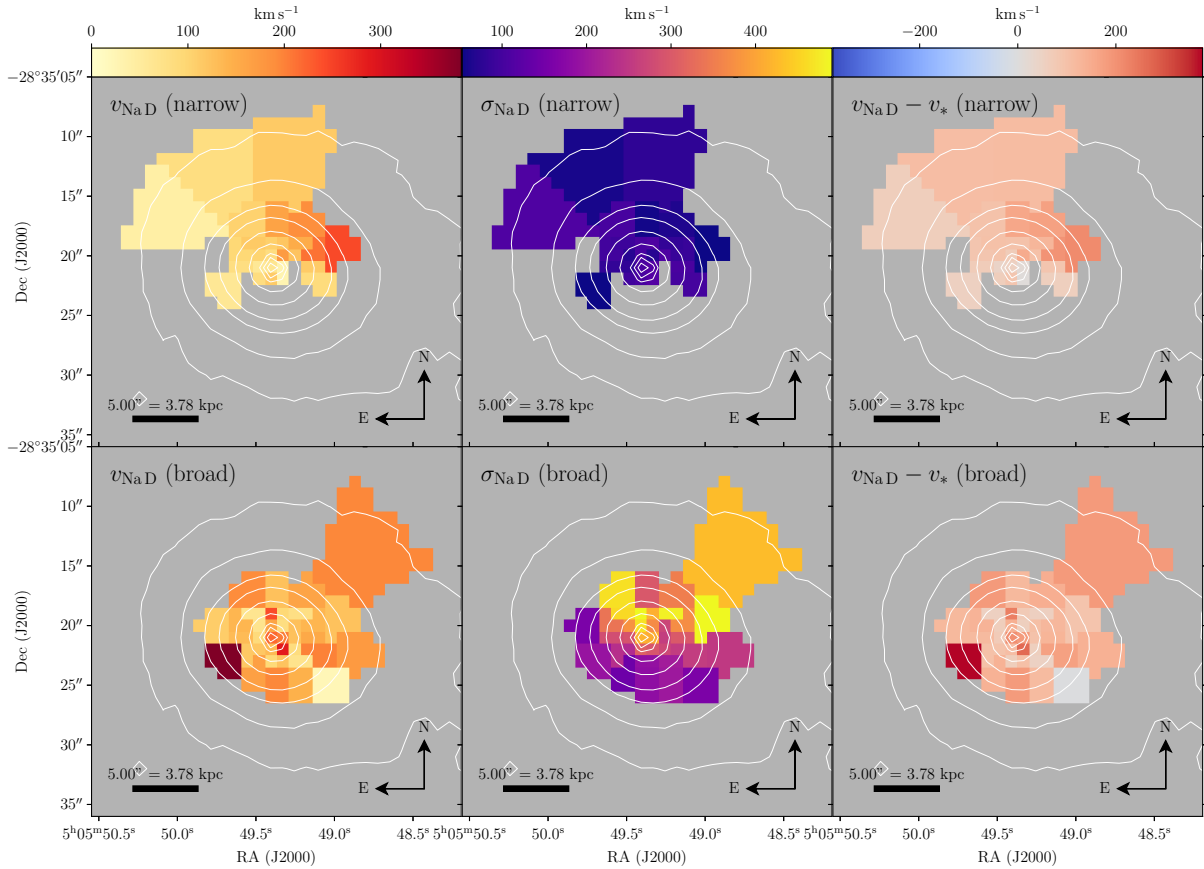


Figure 14. The radial velocity (left) and velocity dispersion (centre) of the narrow (top row) and broad (bottom row) components of the residual Na D absorption. The right column shows the difference between the radial velocity of the Na D and the best-fit stellar population. The contours are as in Fig. 6.

was applied to inflows by [Krug et al. \(2010\)](#), with some caveats which we discuss here.

The inflow was modelled as a mass-conserving flow, such that the mass inflow rate \dot{M} and velocity v are independent of radius. We used the “thin shell” approximation, in which the Na D absorption is assumed to arise from a thin shell of material at a distance r from the galactic centre. Under this assumption, the mass inflow rate averaged over the lifetime of the wind is given by

$$\dot{M} = \Omega \mu m_p N(\text{H}) v r = 4\pi C_\Omega C_f \mu m_p N(\text{H}) v r, \quad (12)$$

where μm_p is the average particle mass (where m_p is the proton mass and $\mu = 1.44$), and $N(\text{H})$ is the H I column density. $\Omega = 4\pi C_\Omega C_f$ is the solid angle subtended by the inflow viewed from the galactic centre, which includes both the large-scale covering fraction C_Ω as well as that representing the clumpiness of the wind, C_f .

For our radius we chose $r = 8$ kpc as it represents the maximum radius at which Na D absorption is detected, and to calculate the large-scale covering fraction of each bin we used $C_\Omega = A_{\text{bin}}/4\pi r^2$ where A_{bin} is the area of the bin projected onto the plane of the sky.

To calculate the hydrogen column density $N(\text{H})$, we first used the expression given by [Spitzer \(1978\)](#) to compute the Na I column density,

$$N(\text{Na I}) = \frac{\tau_{b,0} b}{1.497 \times 10^{-15} \lambda_b f_b} \text{ cm}^{-2} \quad (13)$$

where $f_b = 0.3180$ is the oscillator strength ([Morton 1991](#)). $N(\text{H})$ is

then

$$N(\text{H}) = \frac{N(\text{Na I})}{(1-y) 10^{(a+b_{\text{dep}})}}, \quad (14)$$

where y is the ionisation fraction, a is the Na abundance and b_{dep} is the depletion factor of Na onto dust. Because we could not constrain any of these values from our observations, we assumed $y = 0.9$, solar Na abundance ($a = -5.69$; [Savage & Sembach 1996](#)) and Galactic dust depletion ($b_{\text{dep}} = -0.95$; [Savage & Sembach 1996](#)). $N(\text{H})$ ranges from $10^{20} - 10^{22} \text{ cm}^{-2}$, similar to those measured in samples of radio galaxies with redshifted H I absorption by [van Gorkom et al. \(1989\)](#).

The mass inflow rate in each bin, comprising both broad and narrow absorption components, is then

$$\dot{M}_i = \Omega_i \mu m_p [N_{i,\text{broad}}(\text{H}) v_{i,\text{broad}} + N_{i,\text{narrow}}(\text{H}) v_{i,\text{narrow}}] r. \quad (15)$$

To derive estimates for $N(\text{Na I})$, $N(\text{H})$ and \dot{M} in each bin, we evaluated Eqns. 13, 14 and 15 for each sample of the posterior PDF generated by ULTRANEST. We then estimated central values and errors by computing 16th, 50th and 84th percentiles for the resulting distribution of each parameter. The total mass inflow rates for the narrow and broad components are $\dot{M}_{\text{narrow}} = 1.8^{+0.8}_{-0.6} M_\odot \text{ yr}^{-1}$ and $\dot{M}_{\text{broad}} = 0.4^{+0.4}_{-0.2} M_\odot \text{ yr}^{-1}$, corresponding to a total mass inflow rate $\dot{M} \sim 1 - 3 M_\odot \text{ yr}^{-1}$.

There are many assumptions associated with this calculation. We assumed a “thin shell” geometry such that all of the material is located in a thin shell with a radius of 8 kpc, whereas the increase in

radial velocity of the narrow component towards the West (Fig. 14) may represent gas at smaller radii that has accelerated as it has fallen inwards. Additionally, inflow velocities are likely underestimated as the velocities are projected along the line-of-sight; the true velocity in most bins may be substantially higher. There are also many assumptions in our calculation of $N(\text{H})$, including the Na abundance and ionisation fraction: in particular, because the inflowing gas is likely to be metal-poor (see Section 7.2), our $N(\text{H})$ values are probably underestimated. We estimate these factors to impact the inflow rate by an order of magnitude.

7 DISCUSSION

7.1 The young stellar population

Our ppxf analysis revealed a young ($\lesssim 10$ Myr) stellar population in the Northern regions of ESO 422–G028 with an estimated mass of $10^{7.6} M_{\odot}$. Although low levels of ongoing star formation are common in fast rotator ETGs, this is highly unusual in a slow rotator such as ESO 422–G028 (Shapiro et al. 2010).

Simulations predict that jets can trigger star formation by facilitating instabilities and cloud collapse (Gaibler et al. 2012; Fragile et al. 2004, 2005, 2017). We can safely rule out this scenario in ESO 422–G028; jets tend to inject energy and momentum spherically on kpc scales, thereby leading to a global elevation in the SFR (Mukherjee et al. 2016), in contrast to the relatively localised region of young stars in ESO 422–G028.

It is more likely that the young stellar population formed in-situ after a merger or accretion event. Young stellar populations are found in 15–25 per cent of radio galaxies (Tadhunter et al. 2011), which has been attributed to gas-rich mergers simultaneously triggering star formation and jet activity. Indeed, the estimated mass inflow rate estimated from our Na D observations ($\dot{M} \sim 1 - 3 M_{\odot} \text{ yr}^{-1}$) is sufficient to sustain the observed SFR ($0.4 M_{\odot} \text{ yr}^{-1}$; see Section 5.4). Although ESO 422–G028 shows no obvious morphological disturbances evident of a merger, minor gas-rich mergers can provide fuel for star formation without producing a detectable morphological perturbation (Huang & Gu 2009; Jaffé et al. 2014).

Alternatively, ESO 422–G028 may have acquired the already-formed young stellar populations via a merger. With our current observations, there is unfortunately no way to determine whether the stars were formed in-situ or acquired externally via a merger.

7.2 An inflow of neutral gas

As discussed in Section 5.3, the ionised gas in ESO 422–G028 exhibits dynamically distinct narrow ($\sigma \lesssim 100 \text{ km s}^{-1}$, $v_{\text{rot}} \approx 300 \text{ km s}^{-1}$) and broad ($\sigma \gtrsim 150 \text{ km s}^{-1}$, $v_{\text{rot}} \approx 100 \text{ km s}^{-1}$) kinematic components. The ionised gas is clearly not in equilibrium with the stellar component, which has a maximum LOS rotational velocity of approximately 35 km s^{-1} ; the rotational axes of the stellar and gas components are also offset by approximately 30° in projection.

ESO 422–G028 also exhibits prominent interstellar Na D absorption, a tracer of neutral gas, which is redshifted by up to a few 100 km s^{-1} , thereby tracing infalling gas, as explained in Section 6. Comparison of Figs. 11 and 14 suggests the narrow Na D component may be linked to the ionised gas disk traced by the narrow H α emission, as both the LOS velocities and widths of the narrow-line gas and Na D are similar in the Western half of the galaxy. The Na D absorption is also much deeper in the Northern regions of the galaxy, being entirely absent in the South (see Fig. 12). Similarly localised

regions of redshifted interstellar Na D absorption have recently been observed in radio-active red geysers galaxies (Roy et al. 2021a).

Together, our observations of the ionised and neutral phases of the ISM reveal an inflow of neutral gas streaming from the North, that is settling onto a disk that has become ionised in the interstellar radiation field, fuelling star formation and/or triggering jet activity. Such inflow events are not unusual in ETGs; accretion is suspected to dominate the gas supply for ≈ 40 per cent of ETGs (Davis et al. 2011; Davis & Young 2019). Indeed, misalignments between the gas and stellar kinematics – such as that observed in ESO 422–G028 – are common in ETGs, and are believed to arise from gas accreting into the galaxy at an angle misaligned to the stellar axis of rotation (Bryant et al. 2019).

7.3 Merger or accretion event?

We now investigate possible sources of the inflow into ESO 422–G028. It is highly unlikely that the gas is being accreted from a cosmic filament: as the group is only a projected distance of ~ 1 Mpc from the mega-structure to the North-East (S08), any nearby filaments would preferentially accrete into this more massive structure instead of the small group housing ESO 422–G028. Likewise, the inflow is unlikely to be from a cooling flow in the IGM, as ESO 422–G028, with an X-ray luminosity $L_{0.2-2 \text{ keV}} \sim 10^{41} \text{ erg s}^{-1}$ (S08), lacks the bright X-ray emission associated with such cooling flows (e.g., McNamara & Nulsen 2012; Tremblay et al. 2018). We can also rule out stellar mass loss as the origin of the neutral gas, because the strength of the interstellar Na D absorption is non-uniform across the galaxy, being strongest in the North (Fig. 12). Moreover, its kinematics are highly distinct from that of the stars. The most likely scenario is that the gas is being accreted from a neighbour, or is from a merger with a gas-rich, low-mass galaxy; indeed, the group containing ESO 422–G028 is unvirialised (S08), facilitating interactions between group members.

To investigate these two scenarios, we analysed the formation history of a massive galaxy similar to ESO 422–G028 in the cosmological simulation of Kobayashi & Taylor et al., *in prep*. The simulation is similar to that introduced in Taylor & Kobayashi (2015), using the same initial conditions comprising 240^3 particles of each of gas and dark matter in a cubic box $25 h^{-1}$ Mpc (comoving) per side. The AGN feedback scheme includes formation from dense, metal-free gas, gas accretion assuming the Bondi-Hoyle formalism, isotropic thermal feedback, and black hole mergers (Taylor & Kobayashi 2014). The simulation adopts the updated chemical evolution and stellar feedback model of Kobayashi et al. (2020b), which tracks all individual elements from H to Ge, and includes prescriptions for chemical enrichment and feedback from core-collapse supernovae and AGB winds (Kobayashi et al. 2020b), supernovae Ia (Kobayashi & Nomoto 2009; Kobayashi et al. 2020a), as well as a metallicity-dependent hypernova fraction (Kobayashi et al. 2020b). The simulation assumes the following cosmological parameters: $h = 0.68$; $\Omega_{\text{M}} = 0.31$; $\Omega_{\Lambda} = 0.69$; $\Omega_{\text{b}} = 0.048$.

We identified galaxies at $z = 0$ in this simulation with properties similar to ESO 422–G028. The closest match, which we will refer to as gaX0004, has $M_{*} = 1.5 \times 10^{11} M_{\odot}$, $M_{\text{gas}} = 3.2 \times 10^9 M_{\odot}$, $M_{\text{BH}} = 2.4 \times 10^8 M_{\odot}$, $\text{SFR} = 0.52 M_{\odot} \text{ yr}^{-1}$, and $\dot{M}_{\text{BH}} = 5.7 \times 10^{-5} M_{\odot} \text{ yr}^{-1}$. By matching particle IDs in different snapshots, we follow the gas particles that exist in gaX0004 at $z = 0$ back through the simulation to understand their origin.

Fig. 15 shows the trajectories of these gas particles from $z = 1$ to the present, corresponding to a span of approximately 8 Gyr. Some of

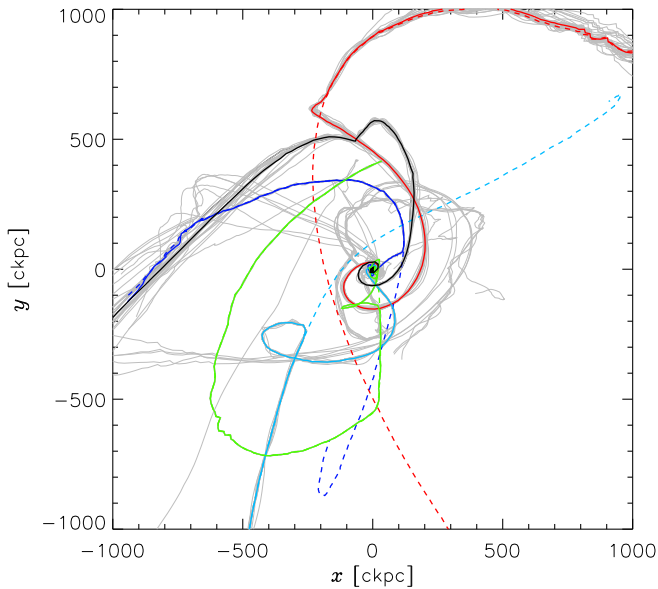


Figure 15. Trajectories of gas particles that are located in the simulated galaxy gaX0004, the closest analogue to ESO 422–G028, at $z = 0$, as well as those of nearby satellite galaxies. Gas particles and galaxies are followed back to $z = 1$. Individual gas particles are shown in grey, important streams of gas are shown by solid coloured lines, and galaxy paths are represented by the dashed lines.

these gas particles are previously associated with low-mass satellites of gaX0004; the motions of the centres of mass of these particles is shown by the solid coloured lines, and the trajectories of their former host galaxies are shown by the equivalently coloured dashed lines. In all four cases the gas is stripped from its galaxy before being accreted by gaX0004, and only one of the satellite galaxies (green in Fig. 15) has merged with gaX0004 by $z = 0$ ⁸. Also shown in black is the path of a coherent, bound mass of gas that falls onto gaX0004, but which is not associated with any galaxy.

Fig. 16 shows the stellar mass, gas mass, SFR and Eddington ratio λ_{Edd} of gaX0004, as well as the galactocentric distance of the gas streams shown in Fig. 15. As expected for a massive galaxy at low redshift, the stellar mass increases only slightly over this period, and both the gas fraction and SFR remain low. However, each gas accretion or merger event is accompanied by first a moderate increase in the SFR, followed by an increase in λ_{Edd} , due to the additional time taken for gas to fall towards the central black hole. In particular, the most recent accretion event has triggered SFRs of approximately $0.5 M_{\odot} \text{ yr}^{-1}$ and Eddington ratios of $\lambda_{\text{Edd}} \sim 10^{-5}$.

These simulations therefore show that both merger events and accretion from either nearby galaxies or the IGM are capable of triggering both star formation and AGN activity at the levels observed in ESO 422–G028. Deep H I observations of the group that could reveal any neutral streams associated with neighbouring galaxies may distinguish whether the gas originated in a satellite galaxy or the IGM. It may also be possible to determine the origin of the gas by measuring its chemistry: whilst the stripped gas has approximately solar metallicity, the material from the IGM is enriched to less than one tenth the solar value. Elemental abundance ratios tell a similar

⁸ Although not important in this context, we note that the gas is removed from these satellites due to interactions with an AGN-driven outflow from gaX0004 itself. Further details can be found in Taylor et al. (*in prep.*).

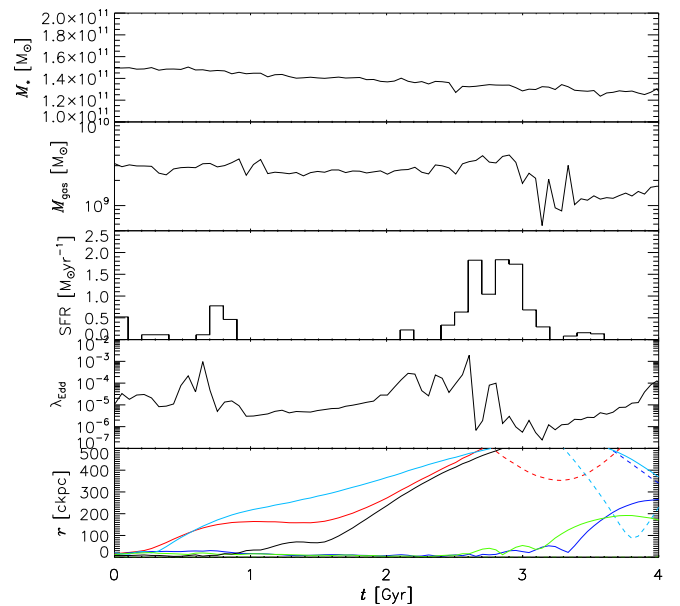


Figure 16. Properties of galaxy gaX0004 over 4 Gyr of lookback time since the present day. From top to bottom, panels show stellar mass, gas mass, star formation rate, Eddington ratio, and the distance of gas streams from gaX0004, where the colours in the bottom panel correspond to the tracks shown in the top panel.

story: the IGM gas is significantly α enhanced, with $[\text{O}/\text{Fe}] = 1.91$ and $[\text{Mg}/\text{Fe}] = 2.35$, compared to ~ 0.5 and ~ 1 , respectively, for the stripped gas. Unfortunately we cannot estimate the metallicity of the inflow without first constraining the total gas mass; similarly we lack the S/N to accurately estimate the metallicity of either kinematic component in the ionised gas.

Interestingly, as shown in Fig. 6, the most recent star formation event began roughly 50–60 Myr ago, whilst the estimated age of the jet is a few Myr (Riseley et al., *in prep.*), implying a time delay of a few tens of Myr between triggering of star formation and the AGN, which is broadly consistent with the delays visible in Fig. 16. However, we note that our stellar age estimates are unlikely to be accurate to within a few 10s of Myr, and so we cannot confidently estimate the length of this delay from our observations.

7.4 What is the evolutionary significance of the inflow?

ESO 422–G028 is undergoing an epoch of restarted jet activity as evidenced by pc-scale jet structures in the nucleus, as well as multiple breaks in the radio-frequency SED, with an estimated age of a few Myr (Riseley et al., *in prep.*).

The comparable timescales of the recent star formation and jet activity may indicate that the inflowing material is responsible for the current epoch of AGN activity. Inflows of neutral gas traced by H I have been reported in radio galaxies (van Gorkom et al. 1989) and may fuel AGN activity; Sato et al. (2009) speculate that these same inflows fuelling “maintenance-mode feedback” may also be observed in Na D. Indeed, localised regions of redshifted interstellar Na D absorption have recently been detected in radio-active red geyser galaxies alongside outflows and low star formation rates, suggesting a link between the inflow, jet activity and feedback (Cheung et al. 2016; Roy et al. 2021b,a).

Although the estimated inflow rate in ESO 422–G028 (\sim

$1 - 3 M_{\odot} \text{yr}^{-1}$) is much higher than those detected in H I ($\sim 0.01 M_{\odot} \text{yr}^{-1}$; van Gorkom et al. 1989), it is within the range of measured Na D-detected inflow rates in radio-active red geyser galaxies ($\sim 0.02 - 5 M_{\odot} \text{yr}^{-1}$; Roy et al. 2021a). Meanwhile, Krug et al. (2010) detected Na D inflows of up to approximately $0.7 M_{\odot} \text{yr}^{-1}$ in roughly a third of their sample of infrared-faint Seyfert galaxies.

It is therefore unclear whether the inflowing gas will form an accretion disk, thereby triggering more powerful Seyfert-like AGN activity via radiatively efficient accretion, or whether it will trigger radiatively-inefficient accretion conducive to powerful jet activity. Radio galaxies have been observed to maintain their LERG status even after the arrival of cold gas (Janssen et al. 2012). Indeed, the observed [O III] luminosity implies radiatively inefficient accretion, with an estimated accretion rate of $\sim 10^{-2} M_{\odot}$ (Section 5.5), although the pc-scale jets may not have yet grown to a size where they can interact with the kpc-scale gas probed by our WiFeS observations. The future state of the radio source in ESO 422–G028 is therefore uncertain.

Davis et al. (2011) predict that newly accreted gas that is misaligned with the existing gas disk will rapidly lose its angular momentum and fall towards the centre of the galaxy due to dissipative collisions between the two components. The inflow in ESO 422–G028 is misaligned with the existing gas disk, as indicated by the presence of two misaligned kinematic components in the ionised gas. Our observations are therefore consistent with a scenario in which the gas is unstable, potentially fuelling star formation and/or nuclear activity as it falls into the centre of the galaxy. The apparent paucity of multiple, misaligned gas disks in ETGs may reflect the short-lived nature of such phenomena.

8 SUMMARY & CONCLUSIONS

We presented our study of ESO 422–G028, a recently restarted giant radio galaxy, using optical integral field spectroscopy from the WiFeS spectrograph. Our findings are summarised as follows:

(i) Unusually for a slow rotator ETG, ESO 422–G028 harbours a young ($\lesssim 10$ Myr) stellar population concentrated in the North-West regions of the galaxy with an estimated mass of $10^{7.6} M_{\odot}$ and an ongoing SFR of $0.4 M_{\odot} \text{yr}^{-1}$.

(ii) ESO 422–G028 also exhibits highly unusual ionised gas kinematics: the H α emission traces two kinematically distinct gas disks, characterised by narrow ($\sigma_{\text{H}\alpha} \lesssim 100 \text{ km s}^{-1}$, $v_{\text{rot}} \approx 300 \text{ km s}^{-1}$) and broad ($\sigma_{\text{H}\alpha} \gtrsim 150 \text{ km s}^{-1}$, $v_{\text{rot}} \approx 100 \text{ km s}^{-1}$) emission lines respectively.

(iii) Prominent redshifted interstellar Na D absorption is present in the North, tracing an inflow of neutral gas with an estimated inflow rate of $1 - 3 M_{\odot} \text{yr}^{-1}$. Both broad ($\sigma_{\text{NaD}} \gtrsim 200 \text{ km s}^{-1}$) and narrow ($\sigma_{\text{NaD}} \lesssim 100 \text{ km s}^{-1}$) components were detected; the narrow component is purely interstellar in origin, whereas the broad component may be contaminated by stellar absorption. Whilst the narrow component appears to be linked to the ionised gas disk traced by the narrow H α emission, the nature of the broad component is less clear.

We propose that ESO 422–G028 is undergoing a minor merger or gas accretion event. The corresponding inflow of gas is occurring from the North, at an angle misaligned with the axis of stellar rotation. The neutral gas has settled into a disk, and may have triggered the observed star formation, resulting in the narrow-line ionised gas disk. This configuration is unstable, as evidenced by kinematic offset between the stars and gas, and will eventually dissipate, resulting in

an inflow of gas towards the centre of the galaxy. The presence of pc-scale jets indicates that at least some of this gas has already made its way to the nucleus, triggering the next epoch of jet activity. This fuelling-starburst-AGN sequence is consistent with the evolution of giant galaxies observed in cosmological simulations.

ACKNOWLEDGEMENTS

The authors thank T. Mendel, G. V. Bicknell, A. Y. Wagner and D. Mukherjee for helpful discussions that improved this work. CJR acknowledges financial support from the ERC Starting Grant ‘DRANOEL’, number 714245 and UM is supported by the Australian Government Research Training Program (RTP) Scholarship. LJK and HRMZ gratefully acknowledge the support of an ARC Laureate Fellowship (FL150100113).

The bulk of this research was carried out at Mount Stromlo Observatory, on the traditional lands of the Ngannawal and Ngambri people, and the observations presented in this work were gathered at Siding Spring Observatory, which is located on the traditional lands of the Gamilaraay/Kamilaroi people.

This research has made use of the NASA/IPAC Extragalactic Database, which is funded by the National Aeronautics and Space Administration and operated by the California Institute of Technology.

This research made use of the PYTHON packages MATPLOTLIB⁹ (Hunter 2007), NUMPY¹⁰ (Harris et al. 2020), SCIPY¹¹ (Jones et al. 2001), and ASTROPY,¹² a community-developed core package for Astronomy (Astropy Collaboration et al. 2013, 2018).

This work used the DiRAC@Durham facility managed by the Institute for Computational Cosmology on behalf of the STFC DiRAC HPC Facility (www.dirac.ac.uk). The equipment was funded by BEIS capital funding via STFC capital grants ST/P002293/1, ST/R002371/1 and ST/S002502/1, Durham University and STFC operations grant ST/R000832/1. DiRAC is part of the National e-Infrastructure.

Stellar models generated with SED@.0 code¹³ with the following inputs: IMF from Salpeter (1955) in the mass range $0.1 - 120 M_{\odot}$; High Resolution library from Martins et al. (2004); González Delgado et al. (2005) based on atmosphere models from PHOENIX (Hauschildt & Baron 1999; Allard et al. 2001), ATLAS9 (Kurucz 1991) computed with SPECTRUM (Gray & Corbally 1994), ATLAS9 library computed with SYNSPEC (Hubeny & Lanz 2011), and TLUSTY (Lanz & Hubeny 2003). Geneva isochrones computed with the isochrone program presented in Meynet (1995) and following the prescriptions quoted in Cerviño et al. (2001) from the evolutionary tracks from Schaller et al. (1992) at $Z = 0.001/Z = 0.020$; Charbonnel et al. (1993) at $Z = 0.004$; Schaerer et al. (1993b) at $Z = 0.008$ and Schaerer et al. (1993a) at $Z = 0.040$. Padova isochrones presented in Girardi et al. (2002)¹⁴ based on the (solar scaled mixture) tracks from Girardi et al. (2000); Bertelli et al. (1994) that includes

⁹ <https://matplotlib.org/>

¹⁰ <https://numpy.org/>

¹¹ <http://www.scipy.org/>

¹² <http://www.astropy.org>

¹³ SED@ is a synthesis code included in the Legacy Tool project of the Violent Star Formation Network; see SED@ Reference Manual at <http://www.iaa.es/~mcs/sed@> for more information.

¹⁴ Available at <http://pleiadi.pd.astro.it/>

overshooting and a simple synthetic evolution of TP-AGB [Girardi & Bertelli \(1998\)](#).

DATA AVAILABILITY

The data underlying this article will be shared on reasonable request to the corresponding author.

REFERENCES

- Allard F., Hauschildt P. H., Alexander D. R., Tamanai A., Schweitzer A., 2001, *ApJ*, **556**, 357
- Allen M. G., Groves B. A., Dopita M. A., Sutherland R. S., Kewley L. J., 2008, *ApJS*, **178**, 20
- Astropy Collaboration et al., 2013, *A&A*, **558**, A33
- Astropy Collaboration et al., 2018, *AJ*, **156**, 123
- Baldwin J. A., Phillips M. M., Terlevich R., 1981, *PASP*, **93**, 5
- Beardsley A. P., et al., 2019, *Publ. Astron. Soc. Australia*, **36**, e050
- Belfiore F., et al., 2016, *MNRAS*, **461**, 3111
- Bertelli G., Bressan A., Chiosi C., Fagotto F., Nasi E., 1994, *A&AS*, **106**, 275
- Bessell M. S., 1999, *PASP*, **111**, 1426
- Best P. N., Heckman T. M., 2012, *MNRAS*, **421**, 1569
- Binette L., Magris C. G., Stasińska G., Bruzual A. G., 1994, *A&A*, **292**, 13
- Boardman N. F., et al., 2017, *MNRAS*, **471**, 4005
- Briggs D. S., 1995, PhD thesis, The New Mexico Institute of Mining and Technology
- Bryant J. J., et al., 2019, *MNRAS*, **483**, 458
- Buchner J., 2014, arXiv e-prints, p. [arXiv:1407.5459](#)
- Buchner J., 2019, *PASP*, **131**, 108005
- Buchner J., 2021, *The Journal of Open Source Software*, **6**, 3001
- Calzetti D., 2013, *Star Formation Rate Indicators*. Cambridge University Press, Cambridge, UK, p. 419
- Cappellari M., 2017, *MNRAS*, **466**, 798
- Cappellari M., Copin Y., 2003, *MNRAS*, **342**, 345
- Cappellari M., Emsellem E., 2004, *PASP*, **116**, 138
- Cerviño M., Gómez-Flechoso M. A., Castander F. J., Schaerer D., Mollá M., Knödseder J., Luridiana V., 2001, *A&A*, **376**, 422
- Charbonnel C., Meynet G., Maeder A., Schaller G., Schaerer D., 1993, *A&AS*, **101**, 415
- Cheung E., et al., 2016, *Nature*, **533**, 504
- Childress M. J., Vogt F. P. A., Nielsen J., Sharp R. G., 2014, *Ap&SS*, **349**, 617
- Condon J. J., Cotton W. D., Greisen E. W., Yin Q. F., Perley R. A., Taylor G. B., Broderick J. J., 1998, *AJ*, **115**, 1693
- Dabhade P., et al., 2020a, *A&A*, **635**, A5
- Dabhade P., et al., 2020b, *A&A*, **642**, A153
- Davis T. A., Young L. M., 2019, *MNRAS*, **489**, L108
- Davis T. A., et al., 2011, *MNRAS*, **417**, 882
- Delhaize J., et al., 2021, *MNRAS*, **501**, 3833
- Dopita M. A., Sutherland R. S., 2003, *Astrophysics of the diffuse universe*. Springer-Verlag Berlin Heidelberg
- Dopita M. A., Sutherland R. S., 2017, *ApJS*, **229**, 35
- Dopita M., Hart J., McGregor P., Oates P., Bloxham G., Jones D., 2007, *Ap&SS*, **310**, 255
- Dopita M., et al., 2010, *Ap&SS*, **327**, 245
- Emsellem E., et al., 2007, *MNRAS*, **379**, 401
- Ferrarese L., Merritt D., 2000, *ApJ*, **539**, L9
- Fitzpatrick E. L., Massa D., 2007, *ApJ*, **663**, 320
- Foreman-Mackey D., 2016, *The Journal of Open Source Software*, **1**, 24
- Fragile P. C., Murray S. D., Anninos P., van Breugel W., 2004, *ApJ*, **604**, 74
- Fragile P. C., Anninos P., Gustafson K., Murray S. D., 2005, *ApJ*, **619**, 327
- Fragile P. C., Anninos P., Croft S., Lacy M., Witry J. W. L., 2017, *ApJ*, **850**, 171
- Gaibler V., Khochar S., Krause M., Silk J., 2012, *MNRAS*, **425**, 438
- Gebhardt K., et al., 2000, *ApJ*, **539**, L13
- Girardi L., Bertelli G., 1998, *MNRAS*, **300**, 533
- Girardi L., Bressan A., Bertelli G., Chiosi C., 2000, *A&AS*, **141**, 371
- Girardi L., Bertelli G., Bressan A., Chiosi C., Groenewegen M. A. T., Marigo P., Salasnich B., Weiss A., 2002, *A&A*, **391**, 195
- González Delgado R. M., Cerviño M., Martins L. P., Leitherer C., Hauschildt P. H., 2005, *MNRAS*, **357**, 945
- Gray R. O., Corbally C. J., 1994, *AJ*, **107**, 742
- Harris C. R., et al., 2020, *Nature*, **585**, 357
- Hauschildt P. H., Baron E., 1999, *Journal of Computational and Applied Mathematics*, **109**, 41
- Heckman T. M., Kauffmann G., Brinchmann J., Charlot S., Tremonti C., White S. D. M., 2004, *ApJ*, **613**, 109
- Huang S., Gu Q. S., 2009, *MNRAS*, **398**, 1651
- Hubeny I., Lanz T., 2011, *Synspec: General Spectrum Synthesis Program* (ascl:1109.022)
- Hunter J. D., 2007, *Computing in Science & Engineering*, **9**, 90
- Jaffé Y. L., et al., 2014, *MNRAS*, **440**, 3491
- Jamrozny M., Machalski J., Mack K. H., Klein U., 2005, *A&A*, **433**, 467
- Janssen R. M. J., Röttgering H. J. A., Best P. N., Brinchmann J., 2012, *A&A*, **541**, A62
- Jarrett T. H., Chester T., Cutri R., Schneider S., Skrutskie M., Huchra J. P., 2000, *AJ*, **119**, 2498
- Jarvis M., et al., 2016, in *MeerKAT Science: On the Pathway to the SKA*. p. 6 ([arXiv:1709.01901](#))
- Jeong H., Yi S. K., Kyeong J., Sarzi M., Sung E.-C., Oh K., 2013, *ApJS*, **208**, 7
- Jones E., Oliphant T., Peterson P., et al., 2001, *SciPy: Open source scientific tools for Python*. <http://www.scipy.org/>
- Jones D. H., et al., 2009, *MNRAS*, **399**, 683
- Kalinkov M., Kuneva I., 1995, *A&AS*, **113**, 451
- Kauffmann G., et al., 2003a, *MNRAS*, **346**, 1055
- Kauffmann G., et al., 2003b, *MNRAS*, **346**, 1055
- Kewley L. J., Dopita M. A., Sutherland R. S., Heisler C. A., Trevena J., 2001, *ApJ*, **556**, 121
- Kewley L. J., Groves B., Kauffmann G., Heckman T., 2006, *MNRAS*, **372**, 961
- Kobayashi C., Nomoto K., 2009, *ApJ*, **707**, 1466
- Kobayashi C., Leung S.-C., Nomoto K., 2020a, *ApJ*, **895**, 138
- Kobayashi C., Karakas A. I., Lugaro M., 2020b, *ApJ*, **900**, 179
- Kormendy J., Ho L. C., 2013, *ARA&A*, **51**, 511
- Krug H. B., Rupke D. S. N., Veilleux S., 2010, *ApJ*, **708**, 1145
- Kurucz R. L., 1991, in *Crivellari L., Hubeny I., Hummer D. G., eds, NATO Advanced Science Institutes (ASI) Series C Vol. 341, Stellar Atmospheres: Beyond Classical Models, Proceedings of the Advanced Research Workshop, Trieste, Italy*. D. Reidel Publishing Co., Dordrecht, p. 441
- Lan T.-W., Prochaska J. X., 2021, *MNRAS*,
- Lanz T., Hubeny I., 2003, *ApJS*, **146**, 417
- Lauberts A., Valentijn E. A., 1989, *The surface photometry catalogue of the ESO-Uppsala galaxies*
- Lehnert M. D., Tasse C., Nesvadba N. P. H., Best P. N., van Driel W., 2011, *A&A*, **532**, L3
- Machalski J., Koziel-Wierzbowska D., Jamrozny M., Saikia D. J., 2008, *ApJ*, **679**, 149
- Mack K. H., Klein U., O'Dea C. P., Willis A. G., Saripalli L., 1998, *A&A*, **329**, 431
- Malarecki J. M., Jones D. H., Saripalli L., Staveley-Smith L., Subrahmanyan R., 2015, *MNRAS*, **449**, 955
- Markwardt C. B., 2009, in *Bohlender D. A., Durand D., Dowler P., eds, Astronomical Society of the Pacific Conference Series Vol. 411, Astronomical Data Analysis Software and Systems XVIII*. p. 251 ([arXiv:0902.2850](#))
- Martins L. P., Leitherer C., Cid Fernandes R., González Delgado R. M., Schmitt H. R., Storch-Bergmann T., Heckman T., 2004, in *Storch-Bergmann T., Ho L. C., Schmitt H. R., eds, IAU Symposium Vol. 222, The Interplay Among Black Holes, Stars and ISM in Galactic Nuclei*. pp 337–338. doi:10.1017/S1743921304002492
- McMahon R. G., Banerji M., Gonzalez E., Kozlov S. E., Bejar V. J., Lodieu N., Rebolo R., VHS Collaboration 2013, *The Messenger*, **154**, 35

- McNamara B. R., Nulsen P. E. J., 2012, *New Journal of Physics*, 14, 055023
- Meynet G., 1995, *A&A*, 298, 767
- Moré J. J., 1978, *The Levenberg-Marquardt algorithm: Implementation and theory*. Springer, Berlin, Heidelberg, pp 105–116, doi:10.1007/BFb0067700
- Morganti R., Oosterloo T., 2018, *A&ARv*, 26, 4
- Morganti R., Tadhunter C. N., Oosterloo T. A., 2005, *A&A*, 444, L9
- Morton D. C., 1991, *ApJS*, 77, 119
- Mukherjee D., Bicknell G. V., Sutherland R., Wagner A., 2016, *MNRAS*, 461, 967
- Offringa A. R., et al., 2014, *MNRAS*, 444, 606
- Park J., Jeong H., Yi S. K., 2015, *ApJ*, 809, 91
- Riffel R. A., Storch-Bergmann T., Winge C., McGregor P. J., Beck T., Schmitt H., 2008, *MNRAS*, 385, 1129
- Roberts-Borsani G. W., Saintonge A., 2019, *MNRAS*, 482, 4111
- Roy N., et al., 2021a, arXiv e-prints, p. arXiv:2106.14901
- Roy N., et al., 2021b, *ApJ*, 913, 33
- Rupke D. S., Veilleux S., Sanders D. B., 2005a, *ApJS*, 160, 87
- Rupke D. S., Veilleux S., Sanders D. B., 2005b, *ApJS*, 160, 115
- Rupke D. S. N., Thomas A. D., Dopita M. A., 2021, *MNRAS*, 503, 4748
- Salpeter E. E., 1955, *ApJ*, 121, 161
- Saripalli L., Gopal-Krishna Reich W., Kuehr H., 1986, *A&A*, 170, 20
- Sato T., Martin C. L., Noeske K. G., Koo D. C., Lotz J. M., 2009, *ApJ*, 696, 214
- Savage B. D., Sembach K. R., 1996, *ARA&A*, 34, 279
- Schaerer D., Meynet G., Maeder A., Schaller G., 1993a, *A&AS*, 98, 523
- Schaerer D., Charbonnel C., Meynet G., Maeder A., Schaller G., 1993b, *A&AS*, 102, 339
- Schaller G., Schaerer D., Meynet G., Maeder A., 1992, *A&AS*, 96, 269
- Schlafly E. F., Finkbeiner D. P., 2011, *ApJ*, 737, 103
- Shapiro K. L., et al., 2010, *MNRAS*, 402, 2140
- Shimwell T. W., et al., 2017, *A&A*, 598, A104
- Singh R., et al., 2013, *A&A*, 558, A43
- Skilling J., 2004, in Fischer R., Preuss R., Toussaint U. V., eds, *American Institute of Physics Conference Series Vol. 735, Bayesian Inference and Maximum Entropy Methods in Science and Engineering: 24th International Workshop on Bayesian Inference and Maximum Entropy Methods in Science and Engineering*. pp 395–405, doi:10.1063/1.1835238
- Skilling J., 2006, *Bayesian Analysis*, 1, 833
- Spitzer L., 1978, *Physical processes in the interstellar medium*, doi:10.1002/9783527617722.
- Subrahmanya C. R., Hunstead R. W., 1986, *A&A*, 170, 27
- Subrahmanyan R., Saripalli L., Hunstead R. W., 1996, *MNRAS*, 279, 257
- Subrahmanyan R., Saripalli L., Safouris V., Hunstead R. W., 2008, *ApJ*, 677, 63
- Sutherland R. S., Dopita M. A., 2017, *ApJS*, 229, 34
- Tadhunter C., et al., 2011, *MNRAS*, 412, 960
- Taylor P., Kobayashi C., 2014, *MNRAS*, 442, 2751
- Taylor P., Kobayashi C., 2015, *MNRAS*, 448, 1835
- Tremblay G. R., et al., 2018, *ApJ*, 865, 13
- Trifalenkov I. A., 1994, *Astronomy Letters*, 20, 215
- Veilleux S., Osterbrock D. E., 1987, *ApJS*, 63, 295
- Wiita P. J., Rosen A., Gopal-Krishna Saripalli L., 1989, *Giant Radio Galaxies via Inverse Compton Weakened Jets*. p. 173, doi:10.1007/BFb0036027
- Willis A. G., Strom R. G., Wilson A. S., 1974, *Nature*, 250, 625
- Zovaro H. R. M., et al., 2020, *MNRAS*, 499, 4940
- van Gorkom J. H., Knapp G. R., Ekers R. D., Ekers D. D., Laing R. A., Polk K. S., 1989, *AJ*, 97, 708

APPENDIX A: EXAMPLE NA D ABSORPTION PROFILE FITS

NaD profile fits and corner plots for two bins, generated using the CORNER package for PYTHON (Foreman-Mackey 2016), showing the posterior parameter distributions sampled by ULTRANEST, are shown

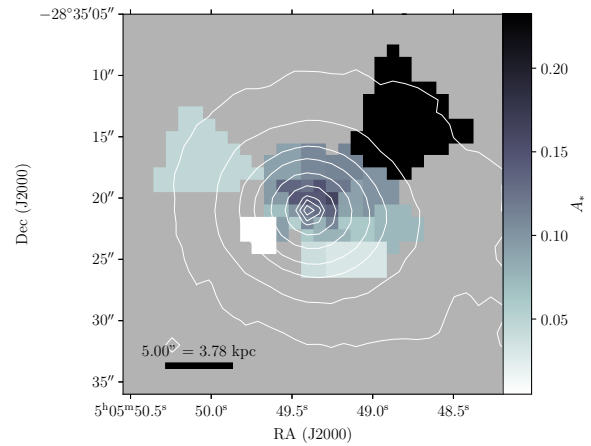


Figure A1. Amplitude A_* of the best-fit residual stellar absorption component in each bin, assuming the broad component is stellar in origin. The contours are as in Fig. 6.

in Figs. A2 and A3. In the former, a two-component fit is preferred, whilst in the latter only a single component is present.

APPENDIX B: ACCOUNTING FOR A POSSIBLE STELLAR COMPONENT IN THE NA D ABSORPTION

To investigate whether the broad residual NaD absorption is stellar in origin, we repeated our analysis detailed in Section 6 using an additional Gaussian absorption component to account for residual stellar absorption. In each bin, a single Gaussian profile was first fitted to the NaD absorption feature in the best-fit stellar continuum obtained from our PPFIT analysis using MPFIT. We then re-ran our absorption profile fit in each bin, substituting a single Gaussian for the broad interstellar component as follows. The absorption profile in each bin was inspected to determine the ideal combination of fitted components: either a single narrow interstellar NaD component, a single stellar Gaussian component, or both, or no profile at all. In those bins where a stellar component was included, a Gaussian absorption component was fitted such that the width and central wavelength of the Gaussian was fixed to that of the stellar template, and only the amplitude A_* was allowed to vary.

The amplitude of the residual stellar absorption component A_* in each bin is shown in Fig. A1. The substitution of the stellar component slightly increased the reduced- χ^2 , but otherwise produced a satisfactory fit to the data in most bins. However, A_* increases significantly from South to North, as shown in Fig. A1. Were the broad component purely stellar in origin, A_* would be relatively uniform across the galaxy; it is therefore unlikely that the broad component is purely stellar in origin.

This paper has been typeset from a $\text{\TeX}/\text{\LaTeX}$ file prepared by the author.

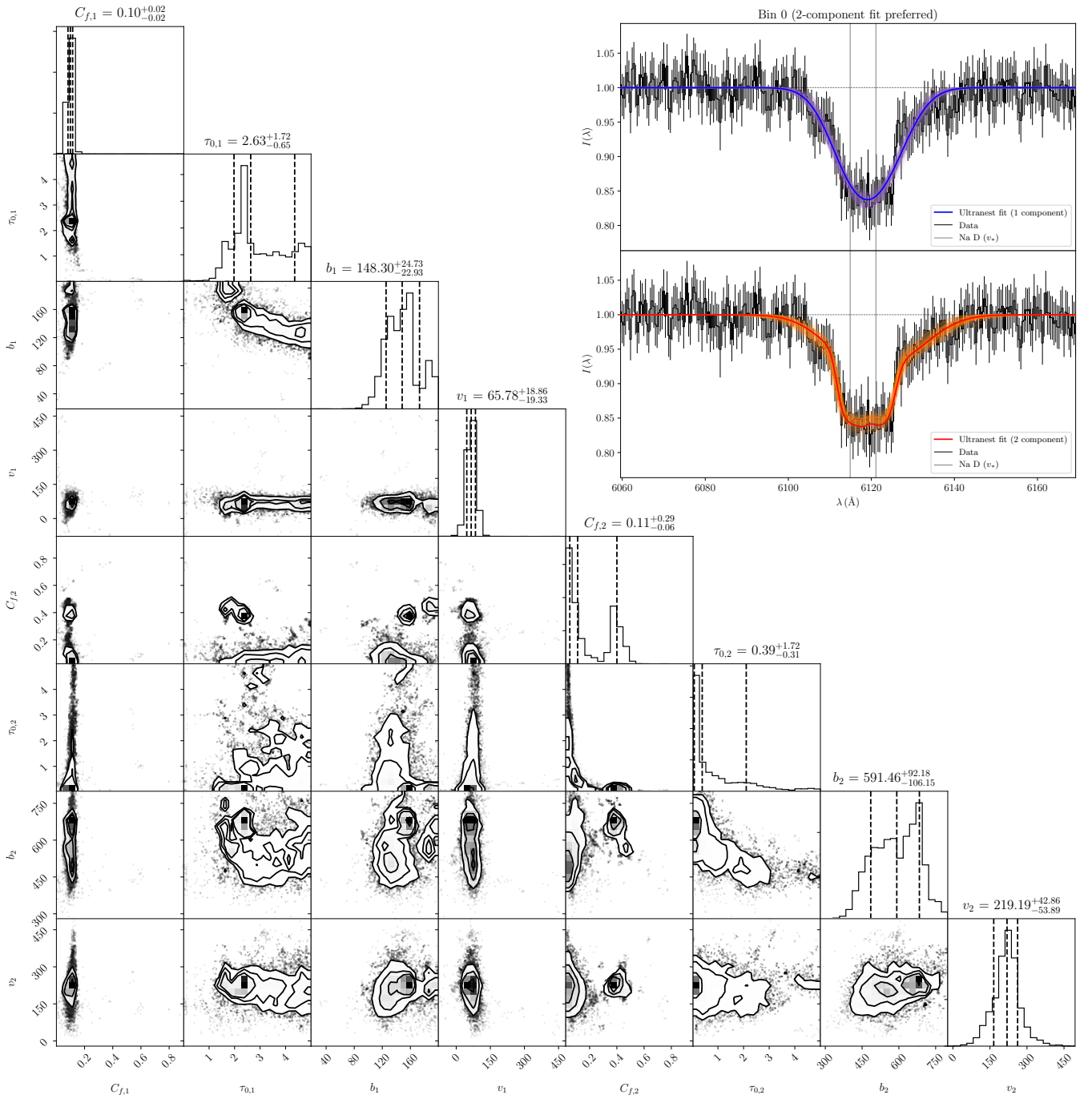


Figure A2. Corner plot showing the posterior PDFs sampled using ULTRANEST corresponding to the Na D absorption profile fit from bin 0 (inset). In the corner plot, the vertical dashed lines indicate 16th, 50th and 84th percentile confidence intervals in the marginalised posterior PDFs. In the inset plot, the upper and lower panels show the fit assuming one and two kinematic components respectively. The pale purple and orange lines show models generated from randomly selected subsets of parameters sampled by ULTRANEST.

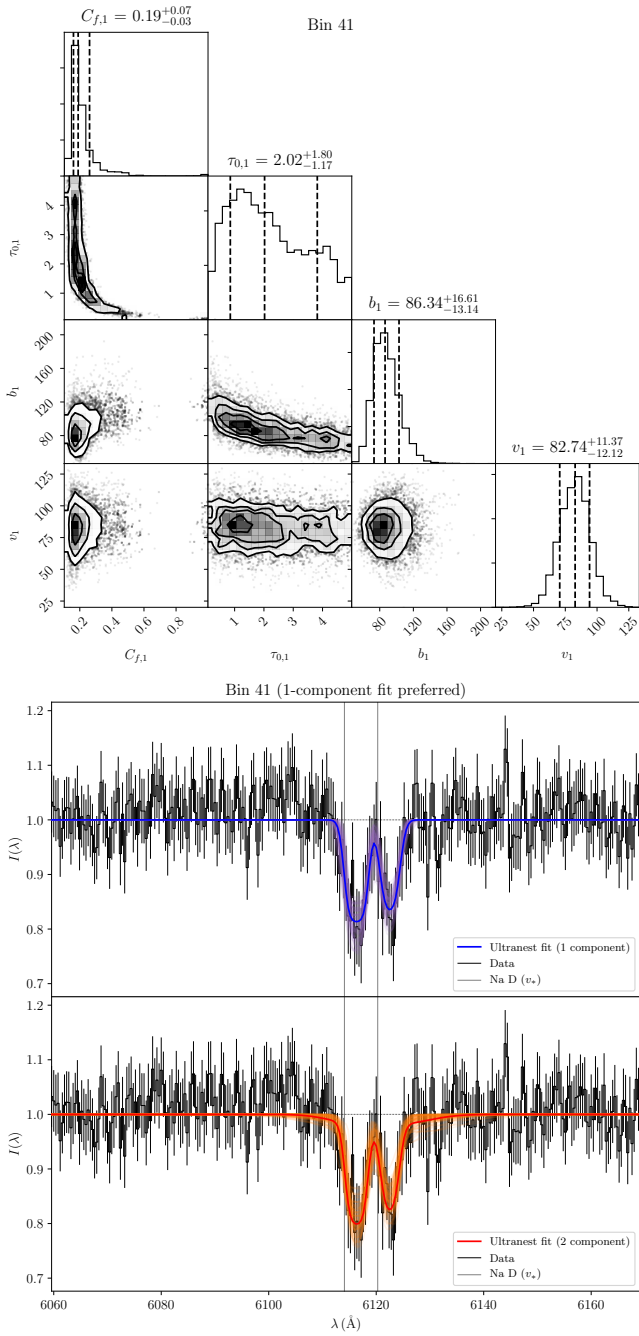


Figure A3. Same as Fig. A2 for bin 41.